ADVANCEMENT AND VERIFICATION OF MOLTRES FOR MOLTEN SALT REACTOR SAFETY ANALYSIS

BY

SUN MYUNG PARK

THESIS

Submitted in partial fulfillment of the requirements
for the degree of Master of Science in Nuclear, Plasma & Radiological Engineering
in the Graduate College of the
University of Illinois at Urbana-Champaign, 2020

Urbana, Illinois

Master's Committee:

Assistant Professor Kathryn D. Huff, Advisor
Associate Professor Tomasz Kozlowski

Abstract

Molten salt reactors, a class of advanced nuclear reactors, promise numerous improvements over the current fleet of largely light-water reactors. As the world continues its transition towards low-carbon electricity generation to combat climate change, building molten salt reactors is a potential option in the near-term future for replacing fossil fuel and aging nuclear power plants. At the current state of development, molten salt reactors still require extensive research to become viable. This thesis presents the latest developments in Moltres, a simulation tool for molten salt reactors. These new developments are: the support for coupling the incompressible Navier-Stokes and the delayed neutron precursor looping systems, and a model for simulating decay heat from fission products at steady-state and during transients. This work demonstrates these capabilities through multiphysics simulations of the Molten Salt Fast Reactor concept. This work first verifies the six-group neutron diffusion results from Moltres against continuous-energy Monte Carlo neutron transport results from Serpent 2. The multiplication factors k_{eff}, delayed neutron fractions β, temperature reactivity coefficient α_T, and the six-group neutron energy spectra from Moltres agreed with the high fidelity simulation results from Serpent 2. The k_{eff} values have small discrepancies on the order of 100 pcm, which is smaller than the -256.7 pcm discrepancy reported in the literature with the same six-group neutron diffusion approach. The decay heat model showed an expected flattening of the temperature distribution due to the movement of the decay heat precursors throughout the primary coolant loop. This work also demonstrates and verifies steady-state and transient multiphysics simulations of the Molten Salt Fast Reactor. The transient scenarios under study include unprotected instances of reactivity insertion, loss of heat sink, loss of flow, and pump overspeed. This thesis verifies the steady-state and transient results against data from the literature for the same case studies. The steady-state temperature and velocity distributions, and the peak neutron flux showed good agreement with the literature results. Minor differences in the delayed neutron precursor distribution and the in-core delayed neutron fraction were explainable with the differences in the handling of turbulence in the models. In three of the transient results (reactivity insertion, loss of heat sink, and pump overspeed), Moltres reproduced the expected magnitude and pattern of the reactor response to these transient initiators. The loss of flow results showed greater discrepancies that resulted from differences in the fluid dynamics modeling in Moltres and the other models. Through the verification studies, this work has also identified avenues for further Moltres software development.

Acknowledgments

I wish to express my deepest gratitude to my advisor, Dr. Kathryn Huff, for her guidance, patience, and encouragement in the past few years. My academic journey thus far has been filled with many ups and downs and it would have been much more difficult without her support. I would also like to thank Dr. Tomasz Kozlowski for his help and invaluable comments as the second reader of this thesis. I wish to acknowledge the funding support from the Singapore Nuclear Safety & Research Initiative under the SNRSI Postgraduate Scholarship program.

I wish to thank my groupmates Dr. Andrei Rykhlevskii, Anshuman Chaube, and Gwendolyn Chee for their input and ideas contributing to the completion of this work. I also greatly appreciate Gavin Davis' and Matthew Kozak's help with proofreading my writing.

Finally, no words can adequately express how thankful I am for my family's unwavering support. I owe a lot to my parents and their efforts for all the opportunities I've benefitted from.

Table of Contents

List of Tables

List of Figures

Chapter 1

Introduction

1.1 Background and Motivation

Greenhouse gas emission from human activities is the main cause of climate change, which has dire consequences on human health and safety due to extreme weather events and the overall impact on food production [1]. Electricity generation from burning fossil fuels represents the greatest source of CO_2 emissions (38% in 2018 [2]); replacing it with low-carbon alternatives would curb a significant fraction of emissions. Nuclear power is a viable low-carbon replacement for burning fossil fuels and it provides consistent base-load power independent of weather and geographical location [3]. Furthermore, employing a diverse mix of nuclear power and renewable sources ensures energy security and reliability in our transition towards a low-carbon future [3].

The world would have to ramp up the current rate of reactor deployments to displace a portion of the presently large share of energy production from fossil fuel power plants. However, several obstacles stand in the way of mass reactor deployments. These obstacles include perceived safety risks, sustainability concerns, nuclear proliferation risks, and the ability to compete economically with other sources of energy [4]. A potential solution to the aforementioned issues is the Molten Salt Reactor (MSR) concept, one of six advanced reactor designs selected by the Generation IV International Forum [5] for continued research and development.

The primary coolants in MSRs consist of molten salt mixtures with fissile and/or fertile material dissolved directly in the coolants. MSRs possess an inherently robust safety feature in the strongly negative fuel temperature coefficient of reactivity. Some designs can also incorporate the thorium fuel cycle for improved sustainability arising from the use of abundant natural thorium resources and reduced transuranic waste. The latter also reduces economical costs associated with long-term nuclear waste storage. In addition, the ability to operate at near atmospheric pressures eliminates the need for a thick pressure vessel and drives down construction costs, while online fuel reprocessing reduces reactor downtime during reactor operation.

However, the liquid fuel form also brings about novel computational challenges in simulating the transient behavior of MSRs; the interactions between neutronics and thermal-hydraulics are stronger due to greater fuel material expansion. Furthermore, fissile material and delayed neutron precursors (DNPs) in MSRs can flow freely within the primary coolant loop as opposed to being held in place in a solid fuel matrix. Therefore, the choice of coupling methods for each set of physics requires careful consideration.

Most reactor analysis applications are usually reactor-specific by design such as TRACE [6] for Light Water Reactors (LWRs), and SAS4A/SASSYS-1 [7] for liquid metal cooled reactors. Thus, these applications would disregard MSR-specific phenomena and are inappropriate for MSR analysis without modifications to the source code. Some research efforts do focus on adapting these applications for MSR analysis. Examples include the coupling of modified versions of TRACE and PARCS [8], and the development of VERA-MSR from the integrated LWR simulation tool VERA [9]. Others developed their MSR simulation tools from general multiphysics or Computational Fluid Dynamics (CFD) applications such as COMSOL [10] and OpenFOAM [11].

Similarly, Moltres [12] is an open-source MSR simulation tool built in the Multiphysics Object-Oriented Simulation Environment (MOOSE) [13] parallel finite element framework. Lindsay et al. [12] first presented the tool in 2017 and demonstrated its capabilities by simulating 2-D and 3-D models of the Molten Salt Reactor Experiment (MSRE). The results showed good qualitative agreement with the original design calculations by MSRE researchers at Oak Ridge National Laboratory (ORNL). This thesis presents some of the new developments in Moltres allowing for more complex and accurate MSR simulations.

1.2 Objectives

This thesis demonstrates latest capabilities of Moltres [12]. In particular, this thesis presents two more recent developments in Moltres, namely fully integrating MOOSE's incompressible Navier-Stokes module into Moltres, and introducing a decay heat model. The main objective of this thesis is to verify Moltres' latest capabilities in modeling multiphysics, steady-state, and transient behavior of fast-spectrum MSRs through the study of the Molten Salt Fast Reactor (MSFR) concept. Code-to-code verification is an important exercise in software development for ensuring that the application produces accurate and reliable results. This thesis covers the MSFR concept mainly because it has been studied extensively with readily available data in the literature to verify against. The MSFR design also features interesting flow patterns that greatly affect the steady-state and transient behavior. This present work will first present a verification of Moltres' MSFR diffusion neutronics against the Monte Carlo neutron transport software Serpent 2, followed by a verification of the coupled neutronics/thermal-hydraulics steady-state and accident transient results against two sets of results published by Fiorina et al. [10]. The two sets of results arose from a collaborative benchmarking exercise by researchers at Politecnico di Milano and Technical University of Delft with two separate MSR simulation tools. Section 2.3 discusses these tools in greater detail. The secondary objective is to identify areas of improvement in Moltres for future development.

1.3 Thesis Outline

The outline of this thesis is as follows. Chapter 2 discusses the history and features of MSRs, and a literature review of existing MSR simulation tools. The chapter also covers the MSFR concept in greater detail. Chapter 3 details the software and the general modeling approach for generating the results in this thesis. Chapter 4 provides a neutronics assessment by comparing key neutronics parameters from Moltres' eigenvalue calculations to Serpent's Monte Carlo calculations. Chapter 5 presents steady-state results of coupled neutronics/thermal-hydraulics MSFR simulations in Moltres. Chapter 6 presents accident transient simulation results for unprotected reactivity insertions, unprotected loss of heat sink, unprotected loss of flow, and unprotected pump overspeed. Lastly, Chapter 7 summarizes the key findings in this thesis and posits some potential avenues for future work.

Chapter 2

Molten Salt Reactors

MSRs are one of six advanced reactor classes shortlisted by the Generation IV Forum in 2001 for promising significant advances in safety, sustainability, efficiency, and cost over existing designs. This attracted significant attention and resources towards MSR research, most noticeable by the number of start-up companies that have emerged in recent years touting various MSR designs. This chapter provides a brief history of MSRs, followed by the distinctive features that earned the concept the label of being a Generation IV reactor. Lastly, this chapter presents the reference specifications of the MSFR concept studied in this work and summarizes the state of the art in the international literature regarding modeling and simulation of the MSFR.

2.1 MSR History

The first MSR, named the Aircraft Reactor Experiment (ARE), dates back to the 1940s as part of the US Aircraft Nuclear Propulsion program [14]. Researchers recommended molten fluoride salts in particular for high uranium solubility, chemical stability, low vapor pressure even at high temperatures, good heat transfer properties, resistance against radiation damage, and reduced corrosive effects on some common structural material [14]. They subsequently built the 2.5 MW_{th} ARE reactor at ORNL, where it achieved criticality on November 1954 and generated 100 MWh over nine days. The fuel consisted of enriched uranium in a molten salt mixture of NaF, ZrF_4, and UF_4. Additionally, the reactor used blocks of BeO for neutron moderation. The aircraft program ultimately never came to fruition as the development of intercontinental ballistic missiles effectively eliminated the need for long-range nuclear-powered bomber aircraft.

However, the successful demonstration of the ARE spurred further research into adapting MSRs for civilian power generation [14]. One key finding from the research was that the thorium fuel cycle had a better breeding ratio than the ^{238}U-to-^{239}Pu fuel cycle in thermal-spectrum reactors. Ultimately, these efforts culminated in the design, construction, and successful operation of the MSRE, a graphite-moderated thermal MSR. The MSRE had a graphite-moderated design with a LiF-BeF$_2$-ZrF$_4$-UF$_4$ fuel salt mixture, initially rated at 10 MW$_{\text{th}}$ but later restricted to 8 MW$_{\text{th}}$ due to a miscalculation of heat transfer capabilities [15]. In January 1969, the MSRE became the first reactor to run on ^{233}U fuel.

Building on their experience with the MSRE, ORNL proposed a new program for the construction and operation of a demonstration reactor based on the Molten Salt Breeder Reactor (MSBR) concept that they had developed [16]. The MSBR is a thermal-spectrum, single fluid reactor with fertile ^{232}Th isotopes mixed directly into the FLiBe molten salt for ^{233}U breeding [17]. Like the MSRE, the MSBR relies on continuous online reprocessing to add fertile material and remove fission product neutron poisons. Researchers estimated the doubling time (the minimum amount of time required to produce enough fissile material to start up another MSBR) to be approximately 22 years. However, ORNL failed to secure funding for the new program in their two attempts in 1972 and 1974. Nevertheless, from a technical perspective, two independent technology evaluation and design studies of the MSR had reported favorably on the promise of the system [16].

In spite of this setback, research into MSRs continued through the late 1970s. In 1980, ORNL published a report describing a new MSR concept, called the Denatured Molten Salt Reactor (DMSR) [17] with denatured ^{235}U fuel (i.e. low-enriched uranium). The ORNL researchers developed this design in response to the fuel reprocessing restrictions introduced by President Ford in 1976. The DMSR would operate as a once-through converter system without fuel reprocessing. While the fuel consists of 19.75 % high-assay low-enriched uranium, the initial core loading includes thorium to boost its conversion ratio throughout its lifetime. It has a continuous online feed consisting of high-assay low-enriched uranium (HALEU) to maintain criticality, and denatured ^{235}U to keep uranium enrichment levels below nuclear non-proliferation policy thresholds. The design also includes a gas sparging system for removing gaseous fission products, while noble metals plate out onto the walls of the coolant loop. The older MSBR design had a significant drawback; the extensive neutron damage in the graphite moderator necessitated frequent replacement (every four years) throughout its operational lifetime. The DMSR avoids this issue by running on a lower power density while maintaining the overall power output of 2250 $\mathrm{MW_{th}}$. As a result, researchers projected that the graphite moderator would last for the entirety of the DMSR's design lifetime.

A concurrent program at the UK Atomic Energy Authority led the development of a 2500 $\mathrm{MW_e}$ lead-cooled Molten Chloride Fast Reactor concept [18]. It is a dual fluid system, with separate loops for the fuel salt and the blanket salt. The blanket is a 1 m-wide tank surrounding the core. The absence of moderators and the choice of chloride over fluoride salt resulted in a relatively hard neutron spectrum which favors ^{239}Pu breeding over the thorium cycle. The UK researchers performed some experiments to study molten salt chemistry but they did not build reactor prototypes. The UK program eventually shut down just like its US counterpart partly due to the successful demonstration of the Prototype Fast Reactor which had achieved criticality in 1974.

Following a lull lasting through the late 20th century, researchers at Centre National de la Recherche Scientifique, the French National Centre for Scientific Research (CNRS) began research into MSRs in 1997 [19]. Starting from the MSBR design, they performed parametric studies based on safety, breeding, and other performance metrics [20]. Their efforts culminated in the MSFR concept, a fast-spectrum breeder MSR designed to run on the thorium fuel cycle [21]. In 2008, the Generation IV International Forum highlighted the MSFR among other MSR designs for further development [22]. The MSFR has also benefited from collaborative research through two European-funded projects, the Evaluation and Viability of Liquid Fuel Fast Reactor System (EVOL) [23] and Safety Assessment of the Molten Salt Fast Reactor (SAMOFAR) [24] projects. Under the EVOL project, researchers further optimized the MSFR design based on neutronic and thermal-hydraulic safety analyses. They also diversified start-up fuel options beyond the original ^{233}U-based fuel composition to include ^{235}U, ^{239}Pu, and transuranic (TRU), and established fuel reprocessing schemes for the MSFR. The SAMOFAR project, which started approximately two years after the end of the EVOL project, supported more comprehensive safety assessments of the reactor and the reprocessing plant, and funded a number of experiments for validation of the MSFR's safety features. This thesis presents steady-state and transient results of the MSFR in Moltres. Therefore, Section 2.4 describes the MSFR design in further detail.

Today, numerous other national and commercial bodies are also developing their own MSR designs. These include the Integral Molten Salt Reactor from Terrestrial Energy [25], the Transatomic Power MSR [26], the Russian Molten Salt Actinide Recycler and Transmuter (MOSART) [27], and the Chinese Thorium Molten Salt Reactor project [28].

2.2 MSR Features

As mentioned in Chapter 1, the most significant difference between MSRs and other reactor concepts is the liquid fuel in MSRs; fissile and/or fertile material is dissolved in high temperature, commonly eutectic mixtures of molten salts. Molten salt-cooled, solid-fuel reactors also exist but this thesis will focus on liquid-fuel reactors. The primary coolant loop containing the fuel salt transfers heat through a heat exchanger to the clean, intermediate loop. The liquid fuel form allows for continuous online fuel reprocessing, and the removal of gaseous fission products via a gas sparging system.

The various MSR designs under development today illustrate the flexibility of this reactor concept. Graphite-moderated thermal-spectrum MSRs are typically straightforward low-enriched uranium (LEU) burners or ^{232}Th/^{233}U breeders, while epithermal- and fast-spectrum MSRs can operate as TRU fuel burners or ^{238}U/^{239}Pu breeders. Breeder designs can be further categorized into one- or two-fluid designs. Two-fluid designs feature separate blanket molten salt mixtures that contain higher proportions of fertile material than the fuel salt mixture. Examples of one-fluid designs include the Integral Molten Salt Reactor [25] and the Transatomic Power MSR design [26] while two-fluid designs include the MSFR [21] and MOSART [27].

2.2.1 Safety

MSRs rely on natural physical phenomena for passive safety such as the strong negative temperature reactivity feedback of the fuel salt due to greater temperature-induced expansion in liquid fuel than solid fuel. Combined with the Doppler broadening of resonance capture cross sections present in both fuel forms, an MSR would see a smaller temperature increase following an unprotected reactivity insertion. The overall temperature reactivity coefficient varies widely among MSR designs due to other structures, such as moderators and reflectors, present in the core. In particular, graphite moderators tend to have slightly positive temperature reactivity coefficients. The MSBR concept has this issue, but the total temperature reactivity coefficient is still relatively large and negative [29]. The negative temperature reactivity feedback provides a great degree of control and stability as it is always present in an MSR regardless of the operating conditions.

Continuous online fuel reprocessing allows operators to maintain low excess reactivity inventories in the core as additional fuel can be added on an ad hoc basis. Reprocessing and gas sparging systems help reduce fissile requirements by continuously removing neutron poisons. These factors, in addition to the strong negative temperature reactivity coefficient, diminish the likelihood and severity of unprotected criticality accidents in MSRs [30]. In the unlikely situation in which an MSR encounters a severe runaway reaction, MSRs rely on another passive safety feature: freeze plugs. Various freeze plugs designs exist for different MSRs. The freeze plug in the MSFR concept is a plug of solidified salt at the bottom of the core actively cooled by fans or other cooling systems to keep its temperature just below the freezing point of the salt [31]. When temperatures in the core exceed a certain threshold during a dangerous transient, the freeze plug melts and drains the molten salt into a containment tank designed to keep the salt in a subcritical configuration. This is especially easy to achieve in thermal-spectrum MSRs as the absence of moderators in the containment tank would automatically drive the multiplication factor down below unity [30].

During pump failure accidents, natural circulation can passively sustain enough heat transfer to remove decay heat and prevent catastrophic structural failure. If natural circulation proves insufficient, the aforementioned freeze plug can drain the salt out of the core. Decay heat in MSRs with online reprocessing is typically lower than that in LWRs due to the continuous removal of fission products. For example, the decay heat in an MSFR after reaching equilibrium salt composition is approximately 3.5% of full reactor power compared to 6% in LWRs [32].

MSRs also typically have a high margin to boiling under nominal operating conditions so that fuel salt boiling is absent [30]. Furthermore, the reactor vessel is consequently subject to much lower stresses as MSRs operate at near-atmospheric pressure levels. Thus, the probability of pipe ruptures due to high pressure is low.

However, MSRs do have some associated safety risks. Firstly, MSRs have smaller fractions of delayed neutron precursors in the active core region as some of the decay in the outer loop regions. This complicates reactor control and may result in faster transients due to the decrease in average neutron lifetime. Secondly, hot molten salts are corrosive and the corrosion mechanism is different from conventional corrosion induced by water and other common agents [33]. The intense gamma and neutron radiation in the core may also accelerate corrosion in the structural components. Lastly, overcooling in pipes and heat exchangers may pose operational challenges as the salt can freeze and restrict flow, causing a loss of flow accident [34].

2.2.2 Other Features

This subsection briefly covers other MSR features that are not the focus of this thesis for completeness.

MSRs have several positive sustainability features. The continuous removal of neutron poisons by the online reprocessing and gas sparging systems creates good neutron economy in MSRs [35]. Both ^{232}Th/^{233}U and ^{238}U/^{239}Pu fuel cycles are viable candidates for breeding in MSRs, with the former being more suited for thermal reactors and the latter being more suited for fast reactors.

The ^{232}Th/^{233}U fuel cycle produces significantly less TRU waste than the other cycles due to the smaller atomic masses of ^{232}Th and ^{233}U. This reduces the overall radiotoxicity and long-term decay heat associated with long-lived plutonium and minor actinide (MA) isotopes. The combination of TRU fuel and ^{232}Th feed in fast spectrum MSRs contributes to lower levels of TRU waste going into long-term storage in nuclear waste repositories [36].

Nuclear non-proliferation concerns in thorium-fueled MSRs involve the separation of the intermediate ^{233}Pa isotope from the fuel salt. ^{233}Pa decays into ^{233}U with a half-life of approximately 27 days and the ^{233}U produced is equivalent in potency to ^{239}Pu for nuclear weapons production [37]. The highly radioactive ^{232}U by-product provides some level of proliferation resistance but nuclear proliferators can sidestep this complication; they can separate the ^{232}U away from the combined ^{232}Pa/^{233}Pa stream after most of the ^{232}Pa has decayed into ^{232}U at a short half-life of 1.31 days [37]. Safeguards by design and close monitoring of MSRs are therefore essential to avoiding spent nuclear fuel diversion.

Economic analyses of MSRs are preliminary at the current stage of MSR development. Qualitatively, many technical factors favor MSRs over LWRs. Some of these factors include: smaller reactor core size due to low operating pressures, higher thermal efficiency and cheaper air-cooling systems due to high operating temperatures, reduction in fuel fabrication costs, and shorter reactor shutdown periods due to online refueling [38].

In terms of technological readiness, MSRs still require significant research efforts and experiments for the validation of various components before a full commercial model can be commissioned. Work towards creating a safety and licensing framework for MSRs has picked up pace only in recent years due to the growing interest from commercial MSR developers.

2.3 Literature Review of MSR Simulation Tools

In the past two decades, researchers have developed several new tools for simulating steady-state and transient behavior in MSRs. Earlier efforts featured simplifications in simulating thermal-hydraulics by using predetermined 1-D velocity fields. One such effort [39] used DYN3D-MSR, an MSR simulation tool adapted from the LWR simulation tool DYN3D while another [40] adapted DALTON, originally a simulation tool for high-temperature reactors. Both works studied the MSRE and simulated flow through advection terms in the temperature and precursor equations in conjunction with full 3-D calculations for neutron flux and heat conduction.

In more recent years, researchers made significant progress towards fully coupled, spatially resolved computational tools that feature 2-D axisymmetric or full 3-D models. In 2011, Cammi et al. [41] performed a "Multi-Physics Modelling" analysis of a simplified 2-D axisymmetric model of a single MSBR fuel channel using the commercial finite element analysis software COMSOL Multiphysics. The physics were implemented through the two-group neutron diffusion equations, and the Reynolds-averaged Navier-Stokes (RANS) standard k-ϵ turbulence model, for the neutronics and thermal-hydraulics respectively. The authors emphasized the need for proper full coupling of the multiphysics and presented both steady-state and transient results in various scenarios such as reactivity insertions, changes in pumping rate, and the presence of periodic perturbations. Nagy et al. [42] introduced an improved version of DALTON which coupled with a CFD application and incorporated incompressible Navier-Stokes flow to simulate salt flow more accurately. The authors validated their model against MSRE experimental data and presented multiphysics simulation results of a different graphite-moderated breeder MSR.

Fiorina et al. [10] adopted both DALTON and the COMSOL-based application in their study of a 2-D axisymmetric model of the MSFR. The authors, from Politecnico di Milano and Technical University of Delft, compared MSFR transient safety analysis results from both tools. They referred to the COMSOL and DALTON/HEAT MSFR models as the Polimi and TUDelft models, respectively, after the universities where each application was developed. This thesis also follows this naming convention. With multigroup neutron diffusion and RANS formulations on ultra fine meshes, both models agreed on the steady-state neutron flux, temperature, and DNP distributions, as well as the power responses following various accident transient initiations. Aufiero et al. [11] concurrently developed a full-core 3-D model of the MSFR in OpenFOAM, albeit with one-group neutron diffusion to reduce computational load. With the 3-D model, the authors could simulate the asymmetric reactor response to the failure of a single pump in the sixteen-pump MSFR configuration. Aufiero et al. also provided quantitative data supporting the use of implicit coupling over explicit coupling to obtain accurate solutions of the transient cases.

Separately, Zhang et al. [43] introduced another self-contained MSR simulation tool named COUPLE. Similar to the COMSOL and OpenFOAM-based models, COUPLE solves the multigroup neutron diffusion equations and the incompressible Navier-Stokes equations with the k-ϵ turbulence model. The authors verified COUPLE's neutronics and thermal-hydraulics against MCNP and a FLUENT-based model, respectively, and presented their multiphysics steady-state results for a 2-D axisymmetric model of the MSFR.

Recognizing the huge computational burden required for full 3-D simulations, some authors came up with innovative ways to alleviate this issue. Zanetti et al. [44] introduced a geometric multiscale modeling approach for various components of a reactor based on the importance of the physical phenomena being simulated. The authors employed a 3-D single-channel model for the MSRE core and modeled the other regions in the reactor such as the upper and lower plenums and the heat exchanger using a lumped parameter approach. They also applied flux factorization to decouple the temporal and spatial components in the neutron diffusion equation. Laureau et al. [45] devised a different method, focusing solely making neutronics calculations more efficient while retaining OpenFOAM's CFD capabilities. The authors adapted fission matrices, commonly used in Monte Carlo neutronics applications, for efficient transient calculations in a modified version of Serpent 2 [46] and coupled it with OpenFOAM for multiphysics transient simulations of the MSFR.

2.4 Molten Salt Fast Reactor

The MSFR is a European reference fast-spectrum MSR concept [20, 21]. Table 2.1 and Figure 2.1 show the main specifications and schematic view of the MSFR, respectively. Developed from the MSBR design, the MSFR is intended to run primarily on a closed thorium fuel cycle with continuous online fuel reprocessing. Several reasons motivated the omission of graphite moderators from the original MSBR design. Firstly, graphite is susceptible to long-term radiation damage and replacement is likely to be necessary during the operating lifetime of the reactor. Secondly, graphite also has a positive temperature coefficient of reactivity; eliminating graphite from the design ensures a greater safety margin [20]. Lastly, while negative temperature coefficients are attainable with extremely thermalized spectra, these configurations require large volumes of graphite which significantly deteriorate breeding ratios due to parasitic absorption [20].

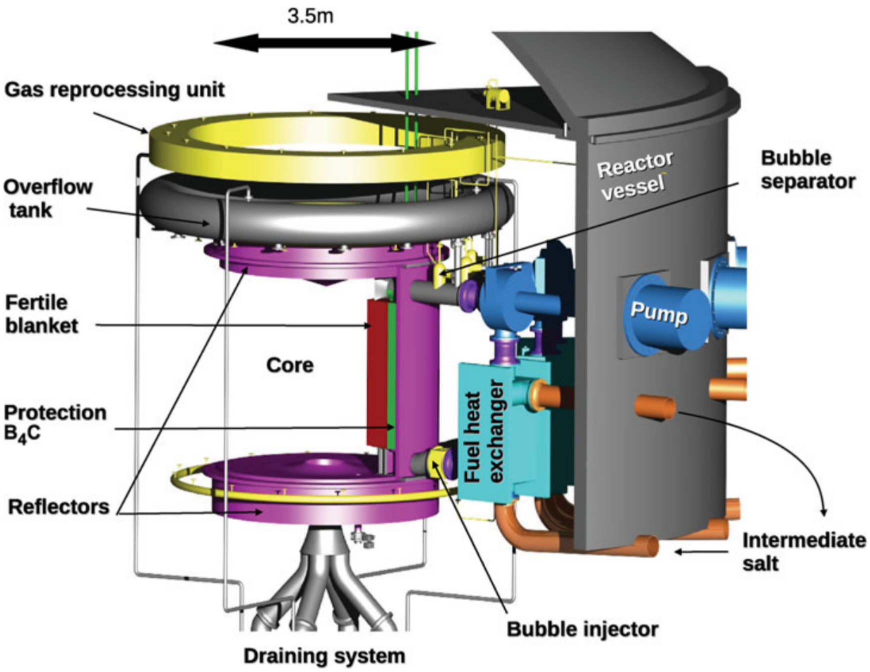

Figure 2.1: Schematic view of the MSFR concept. Figure reproduced from Brovchenko et al. [32].

In the MSFR design, fuel salt flows vertically upward through a 9 m^3 central core region. At the top of the core, the flow separates into sixteen smaller outer loops, each of which passes through a heat exchanger before being pumped back into the bottom of the core. The salt also passes through the online salt reprocessing and gas sparging systems located along the outer loops. A toroidal

Table 2.1: Main specifications of the MSFR concept [47].

Parameter	Value
Thermal/Electric output [MW_{th}/MW_e]	3000 / 1300
Salt volume [m^3]	18
Salt fraction in core	0.5
Number of circulation loops	16
Nominal flow rate [kg s^{-1}]	18500
Nominal circulation time [s]	4.0
Inlet/outlet temperature [K]	923 / 1023
Blanket volume [m^3]	7.3

blanket tank containing fertile salt for breeding surrounds the core radially. The top and bottom of the core are enclosed by nickel alloy reflectors. A layer of boron carbide behind the blanket tank protects the peripheral equipment from excessive neutron damage. During severe accidents when core temperatures rise to dangerous levels, the actively fan-cooled freeze plug at the bottom of the core melts and drains the fuel salt into a containment vessel designed to keep the salt subcritical.

Although the MSFR is primarily designed to operate on the thorium fuel cycle, it supports a range of start-up fuel and feed compositions. This versatility is particularly important for the first few MSFRs to be deployed due to the lack of ^{233}U reserves required for the initial core loading. In general, the fuel and blanket salts are approximately composed of eutectic mixtures of 77.5% LiF - 22.5% AcF_4; AcF_4 represents actinide fluorides such as uranium, thorium, plutonium, and other TRU fluorides. Using fluoride salts instead of chloride salts results in a relatively thermal neutron spectrum. Therefore, the MSFR has a more thermal neutron spectrum than a typical fast-spectrum reactors. For an initial composition consisting of ^{232}Th and ^{233}U, the benchmark value for the amount of ^{233}U for criticality under normal operating conditions is 2.5 mol%. However, a neutronic benchmark study by Brovchenko et al. [48] shows that different neutronics software with different nuclear data provide different k_{eff} estimates even with the same isotopic compositions and temperature distributions. The individual co-authors adjusted the ratio of ^{232}Th to ^{233}U slightly to achieve exact criticality at a uniform temperature of 973 K for their neutronics software [48]. This thesis performs the same exercise to adjust the inlet and outlet temperatures to match nominal values.

The thermal and electric power outputs of the MSFR are 3000 MW $_{th}$ and 1300 MW_e, respectively. The high thermal efficiency ($\eta_{th} = 0.43$) is due to the high operating temperature. The inlet and outlet temperature specifications of the fuel salt are 923 K and 1023 K, respectively, for a minimum 50 K temperature buffer between the operating temperatures and the melting point of the salt (873 K) [23]. The MSFR has heat exchangers and an intermediate molten salt coolant loop to separate the power conversion system from the highly radioactive fuel salt. This also serves as a layer of containment between the radioactive material and the outside environment. The exact composition of the intermediate coolant is not finalized yet but potential candidates include NaF-NaBF$_4$, FLiNaK, LiF-ZrF$_4$, and FliBe [47].

2.4.1 Model Reactor Geometry

The present work uses the same 2-D square-cylindrical MSFR design to compare the present results to results from the Polimi and TUDelft models [10]. The design is a 2-D axisymmetric representation of the MSFR with the sixteen individual outer loops homogenized into a single outer loop as shown in Figure 2.2. For the multigroup group constants calculations in Serpent, the 2-D axisymmetric model is extended into a 3-D model by a 360-degree rotation about the central axis. The material definitions are the same as those specified in the reference MSFR model [48]. Accordingly, the pump and heat exchanger regions are assumed to be composed of 100% fuel salt. While this is an approximation, the outer loop is shielded from the core by a layer of boron carbide and sees sufficiently low neutron fluxes that we may neglect its exact neutronic properties.

Although the present work uses the same 2-D axisymmetric geometry for generating group constant data from Serpent, two minor differences exist between the MSFR geometry modeled herein, and the geometry used in the Polimi and TUDelft models [10]. First, the reactor geometry for Moltres excludes the 2-cm-thick structural material around the blanket tank that separates the fuel and blanket salts. The thickness is much smaller than the rest of the regions in the geometry and it complicated mesh generation in the adjacent regions near the boundaries. The neutronics results in Chapter 4 show that the overall k_{eff} and other parameters from Moltres show good agreement with that from Serpent. It also has no direct impact on the temperature distribution results because the present work solves for the temperature distribution in the primary loop with homogeneous Neumann boundary conditions on the fuel salt-to-wall interface. This approach is for consistency with the Polimi and TUDelft models.

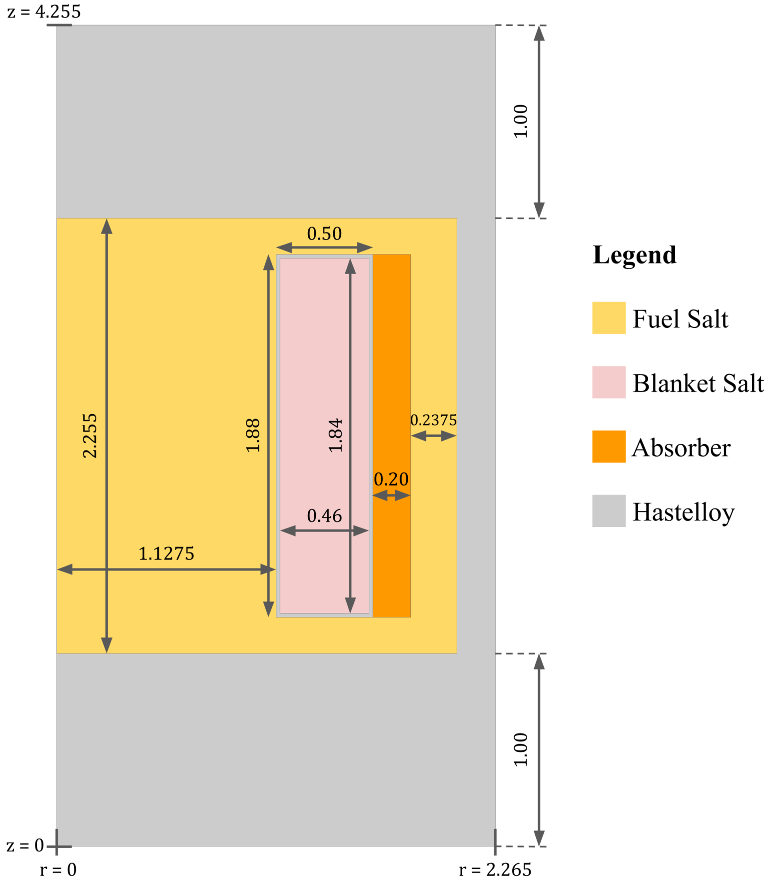

Figure 2.2: 2-D axisymmetric model of the MSFR core used for the simulations in Serpent. All dimensions are in meters. [48]

The second difference pertains to the out-of-core section of the primary loop. The focus for Moltres development has been on core multiphysics over detailed out-of-core multiphysics. The Moltres model simulates the outer loop as a 1-D pipe with a pointwise heat sink to represent the heat exchanger. To simulate the pumps, a Dirichlet boundary condition for inlet velocity drives the flow in the central core region of the primary loop. At every timestep, Moltres converges the core and outer loop calculations using Picard iterations. This approach shares some similarities with the geometric multiscale modeling approach by Zanetti et al. [44]. Future models could create a better representation of the primary loop by implementing a whole continuous loop with pressure increases and drops corresponding to the pumps and heat exchangers.

2.4.2 Material Specifications

This section details the material specifications of the various reactor components in the MSFR.

Molten Salt

The reference start-up salt composition for the fuel and blanket salts is 77.5% LiF - 22.5% AcF_4 (actinide fluorides) [36]. Some researchers working with the MSFR model tweak the exact actinide composition by varying the ^{232}Th to ^{233}U ratio to obtain a k_{eff} value of 1 at a uniform temperature of 973 K [48] or for other purposes [49, 8]. Thus, the exact actinide compositions vary depending on the nuclear data library, neutron transport code, and the purpose of the study. The present work uses a fuel salt composition of 77.5% LiF - 19.913% ThF_4 - 2.587% $^{233}UF_4$ for all calculations, which gives steady-state inlet and outlet temperatures approximately equal to the nominal values in Table 2.1. Table 2.2 shows relevant physical properties of the fuel and blanket salts.

Table 2.2: Properties of the fuel and blanket salts LiF-AcF_4 [48].

Property	Formula	Value at 973 K	Validity Range
Melting temperature [K]	841	N/A	1 bar
Density, ρ [kg m^{-3}]	$4094 - 0.882 \cdot (T - 1008)$	4125	893-1123 K
Dynamic viscosity, μ [Pa s]	$\rho \cdot 5.55 \times 10^{-8} \cdot e^{3689/T}$	0.01015	898-1121 K
Thermal conductivity, k [W m^{-1} K^{-1}]	$0.928 + 8.397 \times 10^{-5} \cdot T$	1.010	891-1020 K
Specific heat, c_p [J kg^{-1} K^{-1}]	$-1111 + 2.78 \cdot T$	1594	867-907 K

Structural Materials

The reflectors on the periphery of the reactor core and the blanket tank are made of a NiCrW Hastelloy (metal alloy) [48], and Table 2.3 details its elemental composition. This alloy has a density of 10 g·cm^{-3}. The MSFR also includes a 20 cm layer of boron carbide (B_4C) to protect the heat exchangers and pumps from neutron irradiation. The reference specifications indicate that natural boron is used, which is composed of 19.8 % ^{10}B and 80.2 % ^{11}B, with an overall density of 2.52 g·cm^{-3}.

Table 2.3: Composition (mol %) of the NiCrW Hastelloy.

Ni	W	Cr	Mo	Fe	Ti	C	Mn	Si	Al	B	P	S
79.432	9.976	8.014	0.736	0.632	0.295	0.294	0.257	0.252	0.052	0.033	0.023	0.004

Chapter 3

Methodology

This work demonstrates the MSFR simulation capabilities of Moltres, a multiphysics simulation tool for MSRs [12]. In particular, this work introduces two new capabilities: full support for coupling incompressible flow with the existing delayed neutron precursor looping capability, and a decay heat model. The former allows users to simulate non-trivial flow patterns in the core and simultaneously loop the precursors through an external region, and the latter to simulate delayed heating from fission products. To run simulations with Moltres, the user must provide group constant data from a neutron transport solver for the multigroup neutron diffusion calculations and a mesh file representing the geometry of the reactor. This work uses Serpent 2 [46] for the former and Trelis/CUBIT [50] for the latter. This chapter provides brief introductions to Serpent 2, MOOSE, and Moltres, and the modeling approach for the MSFR multiphysics simulations in this thesis.

3.1 Serpent 2

Serpent 2 [46] is a continuous-energy Monte Carlo neutron transport application under active development led by the VTT Technical Research Centre of Finland. It was created in 2004 for generating group constants in lattice geometries and has since grown to support more general capabilities. Serpent 2 is highly parallelizable, supporting both MPI and OpenMP parallel programming APIs. It has also been validated and verified against experimental data and other well established neutron transport applications [51].

In Serpent 2, each neutron is tracked through a combination of ray-tracing-based surface tracking and rejection sampling-based delta tracking. Users may define the number of neutron histories and the number of active and inactive cycles for each simulation. Inactive cycles are required for fission source distribution convergence, before interactions are tallied in the active cycles. Interaction types and locations are determined stochastically based on neutron interaction data from established nuclear data libraries (e.g. ENDF [52], JEFF [53]). These nuclear data libraries provide continuous-energy cross section data at discrete temperatures. Beyond the discrete library temperatures, Serpent 2 has a built-in Doppler-broadening preprocessor that extrapolates the relevant cross section data from a lower temperature [46].

Serpent 2 provides standard geometric surfaces (e.g. planes, cylinders, cones) for defining reactor geometries. In this work, the reactor geometry uses the same axisymmetric MSFR geometry as the Polimi and TUDelft models [10], as shown in Fig. 2.2.

3.2 MOOSE

MOOSE [13] is a highly parallelizable, finite element framework developed at Idaho National Laboratory (INL) for simplifying the process of creating fully-coupled, non-linear, multiphysics solvers. The framework provides a user-friendly interface for this task through object-oriented programming in C++. All aspects of a typical multiphysics problem, such as the terms in the partial differential equations (PDEs), the initial and boundary conditions, the material properties, etc., are represented in MOOSE as C++ objects. Child objects can inherit properties from parent objects to simplify implementation and reduce code duplication. Overall, this approach is helpful for many researchers as they are unencumbered by the technical details and complexities involved in programming mesh-handling and PDE-solving in finite element analysis.

MOOSE itself relies on libMesh [54] and PETSc [55] for mesh handling and PDE solver functionalities. As a result, MOOSE supports adaptive meshing schemes and automatic variable scaling, amongst other advanced features in finite element analysis. Full coupling is maintained by the execution of Newton-based solves on the weak formulations of the multiple PDEs to minimize the residual values. Fully-coupled solves are essential for accurately resolving systems with strongly interacting physics. The MSR concept is one such example, in which the neutronics and thermal-hydraulics are tightly coupled through the Doppler effect and the temperature dependence of liquid fuel salt density.

MOOSE, and Moltres by extension, are capable of up to 3-D geometry modeling. They support a wide range of mesh file formats, including the commonly used Exodus II file format. Specifically for 2-D geometries, users can easily switch between Cartesian and polar coordinates by changing one line of code in the input file, without any changes in the Cartesian representations of the PDEs and boundary conditions in their original C++ implementations. This feature provides significant computational time savings for 3-D systems that exhibit high axial symmetry. Another important feature for reducing computational time is the use of MPI for parallel computing. All MOOSE-based applications can be compiled and run on high performance computing clusters.

MOOSE includes a set of built-in physics modules such as the Heat Conduction, Navier-Stokes, and Solid Mechanics modules for commonly studied physical phenomena. This work uses MOOSE's Navier-Stokes module for simulating incompressible salt flow in the MSFR. Peterson et al. verified the incompressible flow capabilities in the Navier-Stokes module and presented results for common CFD problems such as the lid-driven cavity, axisymmetric channel, and flow-over-a-sphere problems [56].

3.3 Moltres

Moltres is an application built in the MOOSE parallel finite element framework [12]. Similar to the physics modules in MOOSE, Moltres contains the necessary kernels representing various physics and boundary conditions for solving for the neutron flux, delayed neutron precursor concentration, and temperature. Together with the Navier-Stokes module, it solves the deterministic multigroup neutron diffusion and thermal-hydraulics PDEs simultaneously on the same mesh. Moltres supports up to 3-D meshes and scales well over a large number of processors. The underlying MOOSE framework provides a range of implicit and explicit methods for the coupling between the neutronics and thermal-hydraulics governing equations.

In the introductory journal article for Moltres, Lindsay et al. [12] demonstrated Moltres' capabilities with 2D-axisymmetric and 3D models of the MSRE. The results showed good qualitative agreement with legacy MSRE data with some minor quantitative discrepancies due to a number of differences in the legacy model. Since then, Moltres has undergone further development in the past three years. The authors of the first paper have since developed various new capabilities in Moltres, most significantly providing support for looping delayed neutron precursors back into the core, and a pointwise heat removal kernel to simulate a heat exchanger. The present author demonstrated these capabilities in an earlier work [57] with a 2-D axisymmetric model of the MSFR with uniform salt flow. The present work also includes these capabilities which are discussed in the following section on the modeling approach.

Building on the prior progress, this thesis presents two more recent developments in Moltres, namely the new features required to couple incompressible flow with the delayed neutron precursor looping capability, and introducing a decay heat model to simulate decay heat from fission products. The incompressible flow profile from MOOSE's Navier-Stokes module provides a more accurate representation of the flow profile, precursor movement, and heat transfer as opposed to assuming uniform velocity fields featured in the previous papers [12, 57]. The next section describes these new developments in detail.

3.4 Modeling Approach

This section discusses the group constant generation in Serpent 2, the neutronics and thermal-hydraulics PDEs that Moltres solves, and the relevant procedures specific to the MSFR model in this work.

3.4.1 Group Constant Generation

The current work uses the JEFF-3.1.2 nuclear data library [53] with Serpent 2 to generate group constants needed by Moltres. The relevant group constant data are collapsed into six neutron energy groups, and calculated at discrete temperature values from 800 K to 1300 K at 100 K intervals. Table 3.1 shows the upper bounds of each neutron energy group. The group constants relevant for neutronics calculations in Moltres are:

Σ_g^f: macroscopic fission cross section in group g,

Σ_g^r: macroscopic removal cross section in group g,

$\Sigma_{g'\to g}^s$: macroscopic scattering cross section from group g' to g,

D_g: diffusion coefficient of neutrons in group g,

ϵ_g: average fission energy per fission by a neutron from group g,

ν: average neutron yield per fission by a neutron from group g,

$\frac{1}{v}$: inverse neutron speed in group g,

λ_i: decay constant of DNP group i,

β_{eff}: effective delayed neutron fraction.

These group constants are extracted from the Serpent 2 output files using a Python script available from the Github repository that holds the Moltres source code [58]. The script rewrites the group constants into a Moltres-compatible format.

Table 3.1: Neutron energy group upper bounds used in Serpent 2.

Group number	Upper bound [MeV]
1	20
2	2.2313
3	0.4979
4	0.024 787 5
5	0.005 530 8
6	0.000 748 5

3.4.2 Central Core Region

As mentioned in the Chapter 2, the fuel salt loop is divided into two regions, the central core region where most of the fissions take place, and the outer loop region where the heat exchanger is located. The red box in Figure 3.1 indicates the central core region. The outer loop is simplified into a 1-D pipe as it is a subcritical region. Its main purposes are to introduce an out-of-core residence time for the DNPs and to contain the heat removal kernel to simulate the heat exchanger. Accordingly, this section provides separate descriptions for the governing equations in the central core region and the outer loop region.

The central core region is of greatest interest to us during steady-state and transient scenarios; the center of the reactor is naturally where most of the fissions and heat generation occur.

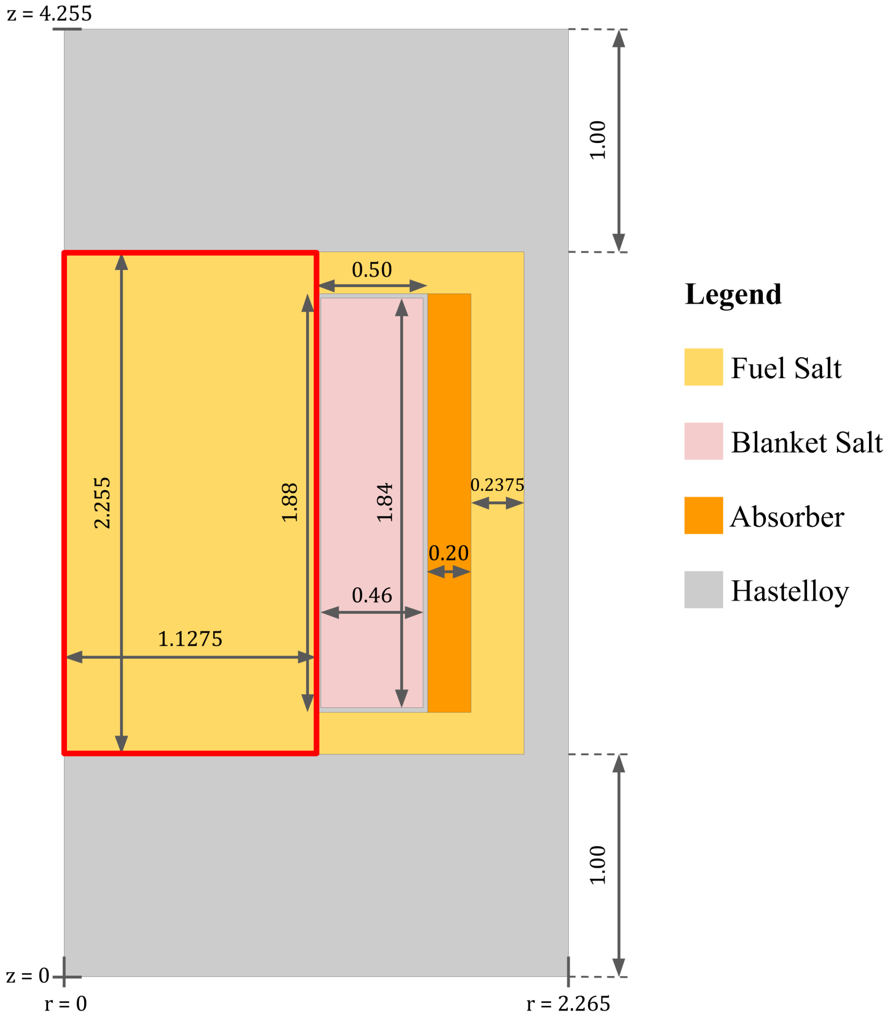

Figure 3.1: 2-D axisymmetric model of the MSFR. The red box indicates the central core region in the modeling approach in Moltres.

Neutronics Model

Moltres performs neutron flux calculations in the central core region using the standard formulations for the time-dependent multigroup neutron diffusion equations and DNP concentration equations as shown in equations 3.1 and 3.2:

$$\frac{1}{v_g}\frac{\partial \phi_g}{\partial t} = \nabla \cdot D_g \nabla \phi_g - \Sigma_g^r \phi_g + \sum_{g' \neq g}^{G} \Sigma_{g' \rightarrow g}^s \phi_{g'} + \chi_g^p \sum_{g'=1}^{G} (1-\beta)\nu \Sigma_{g'}^f \phi_{g'} + \chi_g^d \sum_{i}^{I} \lambda_i C_i, \tag{3.1}$$

$$\frac{\partial C_i}{\partial t} = \beta_i \sum_{g'=1}^{G} \nu \Sigma_{g'}^f \phi_{g'} - \lambda_i C_i - \vec{u} \cdot \nabla C_i + \nabla \cdot K \nabla C_i, \tag{3.2}$$

where

v_g = average speed of neutrons in group g [cm·s^{-1}],

ϕ_g = neutron flux in group g [cm^{-2}·s^{-1}],

t = time [s],

D_g = diffusion coefficient of neutrons in group g [cm^2·s^{-1}],

Σ_g^r = macroscopic cross section for removal of neutrons from group g [cm^{-1}],

$\Sigma_{g' \to g}^s$ = macroscopic cross section of scattering from g' to g [cm^{-1}],

χ_g^p = prompt fission spectrum for neutrons in group g [-],

G = total number of discrete neutron groups [-],

ν = average number of neutrons produced per fission [-],

Σ_g^f = macroscopic fission cross section for neutron in group g [cm^{-1}],

χ_g^d = delayed fission spectrum for neutrons in group g [-],

I = total number of delayed neutron precursor groups [-],

β = total delayed neutron fraction [-],

β_i = delayed neutron fraction of precursor group i [-],

λ_i = average decay constant of delayed neutron precursors in precursor group i [s^{-1}],

C_i = concentration of delayed neutron precursors in precursor group i [cm^{-3}],

K = turbulent diffusion coefficient of the delayed neutron precursors [cm^2·s^{-1}].

While the limitations of the multigroup neutron diffusion method compared to other deterministic and Monte Carlo methods, particularly for flux values near boundaries, are well-documented, the diffusion model provides acceptable accuracy at lower computational costs. Moreover, the central core region contains no material interfaces except at its boundaries. Chapter 4 provides a comparison of the MSFR multiplication factor values and reactivity coefficients between Moltres and Serpent.

The DNP concentration equation has additional advection and turbulent diffusion terms to account for the movement of DNPs in the primary coolant loop. The turbulent diffusion K is governed by the following equation:

$$K = \frac{\mu_t}{\rho Sc_t} \tag{3.3}$$

where

$\mu_t =$ eddy viscosity [Pa s],

$\rho =$ density of the fuel salt [kg m^{-3}],

$Sc_t =$ turbulent Schmidt number [-].

This work assumes $Sc_t = 0.85$ for a fair comparison with the Polimi and TUDelft models [10] which used the same value. It has its roots in the Reynolds Analogy, which states that turbulent momentum and heat transfer largely depend on the same eddies in turbulent flow [59]. Therefore, Sc_t should be close to unity. $Sc_t = 0.85$ is also the default value for most commercial CFD software [59].

Moltres users can use an arbitrary number of neutron energy groups as long as they provide Moltres with the appropriate group constant data. The number of precursor groups is also variable, though usually predetermined by the choice of nuclear data library in the group constant generation step. Moltres automatically interpolates the group constant data for required temperatures using one of the many predefined interpolation methods available in MOOSE. Once again, Moltres allows users to select their interpolation method of choice.

This work uses six neutron energy groups according to the energy boundaries in table 3.1, and eight DNP groups as defined by the JEFF-3.1.2 library. The neutron flux and DNP concentration values were approximated by first-order Lagrange and constant monomial shape functions respectively on the finite element mesh. Figure 3.2 shows the mesh adopted for the MSFR model. This work assumes vacuum boundary conditions for all six neutron group fluxes along the external boundaries of the geometry, and homogeneous Neumann boundary conditions along the axial symmetry boundary. For the DNP concentrations, this work imposed homogeneous Neumann boundary conditions on the walls, and inflow and outflow boundary conditions on the inlet and outlet boundaries, respectively.

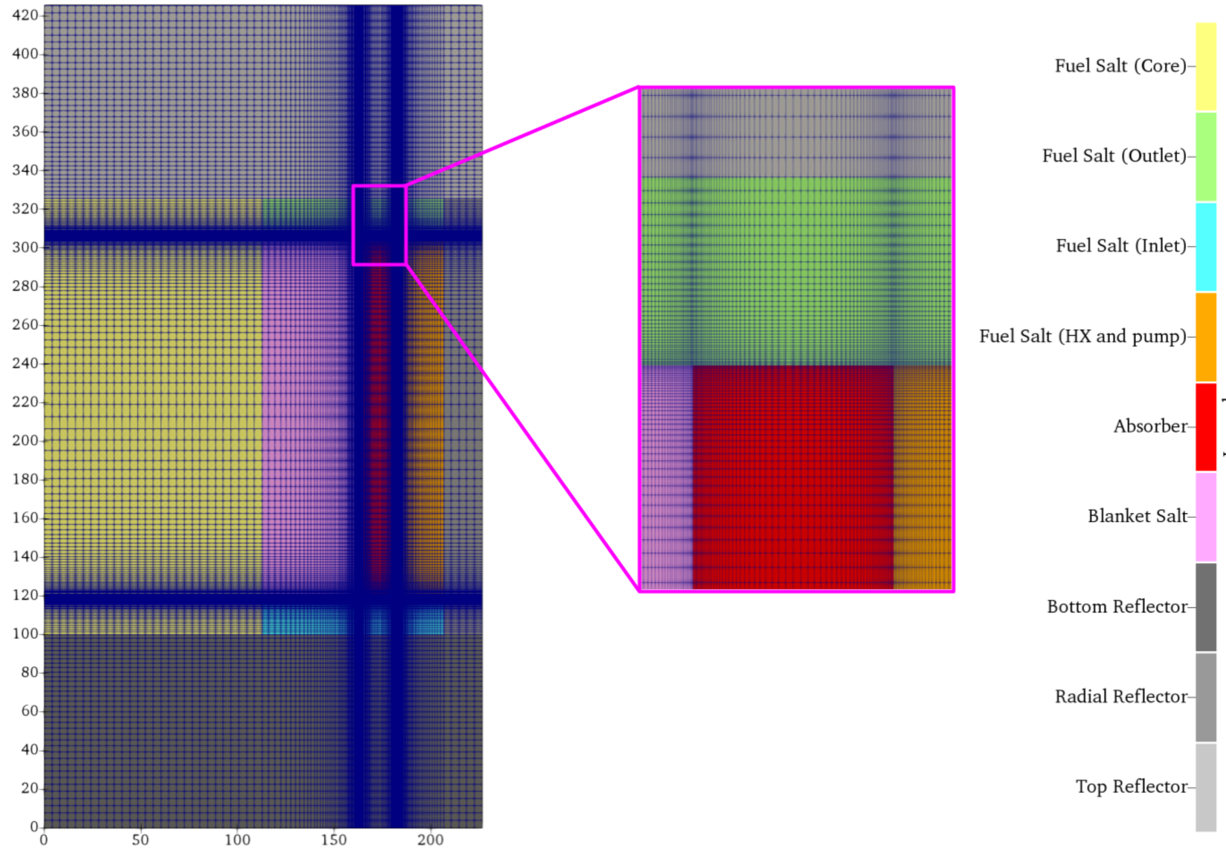

Figure 3.2: Mesh adopted in Moltres and a close-up view of the mesh around the boron carbide absorber.

The inlet DNP concentration values were imported from the outlet values of the 1-D outer loop pipe at the same timestep. Table 3.3 describes these boundary conditions mathematically.

For the decay heat model, a previous study on the MSFR by Aufiero et al. [60] showed that using three decay heat precursor groups with appropriate half-lives in the form of exponential equations, can accurately model decay heat in the MSFR for up to 300 seconds after shutdown with a relative error of less than 2%. Thus, this thesis implements the new decay heat modeling capability with the following equation:

$$\frac{\partial \omega_j}{\partial t} = f_j \sum_{g=1}^{G} \epsilon_g \Sigma_g^f \phi_g - \lambda_j \omega_j - \vec{u} \cdot \nabla \omega_j + \nabla \cdot K \nabla \omega_j, \tag{3.4}$$

where

$\omega_j =$ total decay heat power density from decay heat precursors in group j [W·cm^{-3}],

$f_j =$ fraction of total power attributable to decay heat group j [-],

$\epsilon_g =$ average fission energy per fission initiated by a neutron in group g [W],

$\lambda_j =$ average decay constant of decay heat precursors in group j [s^{-1}].

Like the neutron energy and DNP groups, Moltres can accommodate an arbitrary number of decay heat groups. The current work uses the same decay heat fractions and decay constants, shown in Table 3.4, used in the Polimi and TUDelft models for three decay heat groups.

Table 3.2: Decay heat group parameters [10].

Decay heat group j	λ_j [s^{-1}]	f_j
1	0.1974	0.0117
2	0.0168	0.0129
3	0.000 358	0.0186

Thermal-Hydraulics Model

This work models fluid dynamics using the incompressible Navier-Stokes (INS) capabilities from the MOOSE Navier-Stokes module [56]. The standard INS equations are:

$$\text{Momentum eq.:} \qquad \rho\frac{\partial \vec{u}}{\partial t} = -\rho(\vec{u}\cdot\nabla)\vec{u} + \nabla\cdot[-p\vec{I} + \mu[\nabla\vec{u} + (\nabla\vec{u})^T]] + \vec{f} \tag{3.5}$$

$$\text{Divergence-free:} \qquad \nabla\cdot\vec{u} = 0 \tag{3.6}$$

where

$p =$ pressure [Pa],

$\mu =$ dynamic viscosity [Pa·s],

$\vec{f} =$ body force per unit volume [N·m^{-3}].

In addition to the intrinsic molecular viscosity in the INS equations, this thesis includes an eddy viscosity term, μ_t, to approximate turbulent flow effects. The current implementation of the Navier-Stokes module does not have a turbulence model. The options for turbulence modeling in CFD include direct numerical simulations (DNS) and large eddy simulations (LES) for higher fidelity flow simulations, RANS methods for balanced compromises between accuracy and computational speed, and lumped parameter and sub-channel methods for even faster performance with greater accuracy costs [61]. The Polimi and TUDelft models used RANS methods to model salt flow [10]. This work uses a zeroth-order approximation of μ_t based on the calculated μ_t values reported in the Polimi and TUDelft models. The models predicted spatial μ_t values ranging from 0 to 110 Pa·s, with most values falling within the 30 to 50 Pa·s range. Thus, the present work uses the approximated value $\mu_t = 40$ Pa·s. Despite the simplicity of this approximation, the resulting flow profile is similar to the flow profile in the Polimi and TUDelft models at steady-state.

The energy balance equation for temperature used in this Moltres model is:

$$\rho c_p \frac{\partial T}{\partial t} = -\rho c_p \vec{u} \cdot \nabla T + \nabla \cdot \left[(k + k_t) \nabla T \right] + Q_s \tag{3.7}$$

$$k_t = \frac{\mu_t}{\rho Pr_t} \tag{3.8}$$

$$Q_s = \Big(1 - \sum_{j=1}^{J} f_j\Big) \sum_{g=1}^{G} \epsilon_g \Sigma_g^f \phi_g + \sum_{j=1}^{J} \omega_j, \tag{3.9}$$

where

c_p = specific heat capacity of molten salt [J·kg^{-1}·K^{-1}],

T = temperature of molten salt [K]

$\vec{u}$ = velocity of molten salt [m·s^{-1}],

k = thermal conductivity of molten salt [W·m^{-1}·K^{-1}],

J = total number of decay heat groups [-].

The diffusion term includes turbulent heat diffusivity based on the eddy viscosity μ_t and the turbulent Prandtl number Pr_t. Pr_t is also 0.85 due to the same reasoning provided for Sc_t. The first term in the heat source Q_s equation represents prompt fission heat, and the second term represents decay heat from the J decay heat groups.

With this model, the results were expected to show good qualitative agreement with the Polimi and TUDelft models, including the large recirculation region near the blanket tank walls and the resulting high temperatures in that region. The results in Chapter 5 show minor discrepancies in regions where the viscosity values were under- or over-predicted.

Boundary Conditions

Table 3.3 summarizes the boundary conditions for all variables on all of the relevant boundaries. Figure 3.3 shows the locations of the various boundaries listed in the table. The CoupledOutflow boundary condition for C_i and ω_j is a new feature in Moltres that allows users to couple these variables to the outlet velocity components (e.g. u_x, u_y). Without this boundary condition, users could only use uniform or fixed function-based velocity profiles in conjunction with the precursor looping capability.

Table 3.3: Boundary conditions in the main reactor geometry (Figure 3.3).

Variable	Boundary	Boundary Condition
Neutron flux ϕ_g	Top	$\frac{d\phi_g}{dx}\Big\|_{\text{inflow}} = 0$
	Outer	$\frac{d\phi_g}{dx}\Big\|_{\text{inflow}} = 0$
	Bottom	$\frac{d\phi_g}{dx}\Big\|_{\text{inflow}} = 0$
	Axial	$\frac{d\phi_g}{dx} = 0$
Delayed neutron precursor concentration C_i	Top (Core)	$\frac{dC_i}{dx} = 0$
	Bottom (Core)	$\frac{dC_i}{dx} = 0$
	Outer (Core)	$\frac{dC_i}{dx} = 0$
	Axial (Core)	$\frac{dC_i}{dx} = 0$
	Inlet (Core)	$C_i = c$
	Outlet (Core)	$u_x \cdot C_i = 0$
Decay heat power density ω_j	Top (Core)	$\frac{d\omega_j}{dx} = 0$
	Bottom (Core)	$\frac{d\omega_j}{dx} = 0$
	Outer (Core)	$\frac{d\omega_j}{dx} = 0$
	Axial (Core)	$\frac{d\omega_j}{dx} = 0$
	Inlet (Core)	$\omega_j = c$
	Outlet (Core)	$u_x \cdot \omega_j = 0$
Radial velocity u_x	Top (Core)	$u_x = 0$
	Bottom (Core)	$u_x = 0$
	Outer (Core)	$u_x = 0$
	Axial (Core)	$u_x = 0$
	Inlet (Core)	$u_x = c$
	Outlet (Core)	$\frac{du_x}{dx} = 0$
Axial velocity u_y	Top (Core)	$u_y = 0$
	Bottom (Core)	$u_y = 0$
	Outer (Core)	$u_y = 0$
	Axial (Core)	$\frac{du_y}{dx} = 0$
	Inlet (Core)	$u_y = 0$
	Outlet (Core)	$\frac{du_y}{dx} = 0$
Temperature T	Top (Core)	$\frac{dT}{dx} = 0$
	Bottom (Core)	$\frac{dT}{dx} = 0$
	Outer (Core)	$\frac{dT}{dx} = 0$
	Axial (Core)	$\frac{dT}{dx} = 0$
	Inlet (Core)	$T = c$
	Outlet (Core)	$\frac{dT}{dx} = 0$

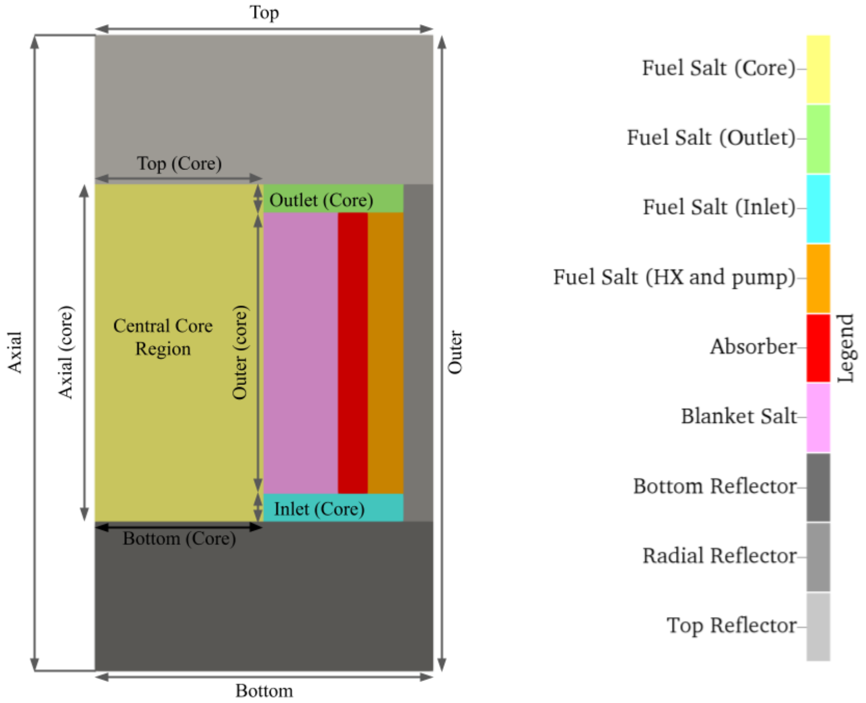

Figure 3.3: The boundaries in the MSFR geometry that are relevant for the boundary conditions mentioned in Table 3.3.

3.4.3 Outer Loop Region

Moltres also accounts for the decay of DNPs outside the central core region by simulating its flow in a separate 1-D pipe geometry. This outer loop pipe calculation is implicitly coupled to the active core simulation through Picard iterations in MOOSE's MultiApp functionality and inlet/outlet boundary values. For this work with the MSFR model, the pipe length is 2.255 m with salt flowing at 1.1275 m s^{-1} for an out-of-core residence time of 2 s. The present author derived these parameters from the reference specifications of 4s cycle time and 50% out-of-core salt fraction (Table 2.1).

Neutronics Model

The outer loop region is largely subcritical because most of it is adjacent to the boron carbide absorber as shown in Figure 3.1. Therefore, the only significant neutronics-related phenomena are the drift and decay of DNPs. The governing equation for the DNPs is:

$$\frac{\partial C_i}{\partial t} = -\lambda_i C_i - u\frac{\partial C_i}{\partial x}. \tag{3.10}$$

Equation 3.10 is derived from equation 3.2 by removing the fission DNP source term, and the conversion of the advection and diffusion terms to their 1-D forms. The decay constants and diffusion coefficient are the same values used in the central core region.

Thermal-Hydraulics Model

A constant velocity of 1.1275 m s^{-1} is applied in the outer loop region to maintain the nominal 2s out-of-core residence time. The governing equation for temperature, derived from equation 3.7, is:

$$\rho c_p \frac{\partial T}{\partial t} = -\rho c_p u \frac{\partial T}{\partial x} - Q_{hx} \tag{3.11}$$

$$Q_{hx} = \alpha (T - T_i) \delta(x_0) \tag{3.12}$$

where

Q_{hx} = heat removal rate through the heat exchanger [W],

α = heat transfer coefficient [W·K^{-1}],

T_i = temperature of the intermediate salt [K],

x_0 = position of the point heat exchanger [m].

In the outer loop region, the fission heat source term is replaced with a heat exchanger sink term Q_{hx} which depends on the temperature difference between the fuel salt T and the intermediate loop salt T_i. For simplicity, this work assumes a constant temperature of 823 K in the intermediate loop. The heat transfer coefficient was determined by assuming that the fuel outlet temperature is 1023 K and calculating the heat removal rate to induce a 100 K drop at the given volumetric flow rate and heat capacity of the fuel salt. The resulting value for α is 370.668 W·K^{-1}. This work opted to ignore the diffusion term due to the discontinuity of the temperature distribution across the point heat exchanger.

Boundary Conditions

Table 3.4 summarizes the boundary conditions for all variables on the inlet and outlet of the 1-D outer loop region. The inlet boundary conditions are all Dirichlet boundary conditions. The inlet boundary values are set by the outflow from the central core region that this inlet is connected to in the actual reactor geometry. The outlet boundary conditions are all outflow boundary conditions as shown in Table 3.4.

Table 3.4: Boundary conditions in the 1-D outer loop geometry. u represents the 1-D velocity in this region.

Variable	Boundary	Boundary Condition
Delayed neutron precursor concentration C_i	Inlet (Core) Outlet (Core)	$C_i = c$ $u \cdot C_i = 0$
Decay heat power density ω_j	Inlet (Core) Outlet (Core)	$\omega_j = c$ $u \cdot \omega_j = 0$
Temperature T	Inlet (Core) Outlet (Core)	$T = c$ $u \cdot T = 0$

3.4.4 Central Core and Outer Loop Coupling

This subsection details the delayed neutron and decay heat precursors, and temperature coupling between the central core and outer loop regions.

This work uses a parabolic flow profile on the inlet Dirichlet boundary condition. The equation for u_x at the inlet is:

$$u_x = -\xi\left[\frac{y}{H} - \left(\frac{y}{H}\right)^2\right] \tag{3.13}$$

where

$\xi =$ normalizing constant [m$\cdot$s^{-1}],

$y =$ height along the inlet [m],

$H =$ total height of the inlet $= 0.1875$ m.

ξ is a normalizing constant that depends on the total volumetric flow rate, $\dot{V}$. Solving the following set of equations in v and $\dot{V}$:

$$v = \xi[\frac{y}{H} - \frac{y^2}{H^2}] \tag{3.14}$$

$$\dot{V} = \int_0^h \int_0^{2\pi} vrd\theta dy \tag{3.15}$$

where

$r =$ radius [m],

$\theta =$ azimuthal angle [rad],

gives $\xi = 20.3401$ m·s^{-1} for $\dot{V} = 4.5$ m^3·s^{-1}.

At every timestep, Moltres also calculates weighted averages of the temperature and the precursors at the outlet. These values are weighted by the outflow velocity values at the outlet according to the following equation:

$$\overline{\psi} = \frac{\int_{\mathcal{C}} \psi(y)u(y)dy}{\int_{\mathcal{C}} u(y)dy} \tag{3.16}$$

where

$\psi =$ variable to be weighted [-]

$\mathcal{C} =$ outlet boundary area [-]

$u =$ outflow velocity perpendicular to the outlet boundary [m·s^{-1}].

Moltres transfers this outflow value from the central core region to the 1-D outer loop region, to be used as the boundary value for the inhomogeneous Dirichlet boundary condition at the inlet. Likewise, the outflow value from the outer loop region is used for the inflow value in the central core region. No averaging is required for this step as the outer loop region is a 1-D system. We assume that the inflow temperature and DNP are uniform at the inlet. The Picard iterations within every timestep ensure that the two systems are implicitly coupled even though they're solved separately.

Chapter 4

Neutronics Results

This chapter verifies Moltres' ability to reproduce key neutronics parameters using group constant data from Serpent 2, which is essential for accurate neutronics calculations in the subsequent multiphysics simulations. The model under study is a static model of the MSFR, i.e. no salt flow, and uniform temperature distribution to assess the accuracy of the six-group neutron diffusion model in Moltres on a fast-spectrum reactor. Table 4.1 lists relevant details of the static MSFR model in Moltres. This verification exercise builds on the previous study by Lindsay et al. [12] that verified Moltres' neutronics capabilities with a two-group neutron diffusion model of the MSRE.

Table 4.1: Details of the static MSFR model in Moltres.

Detail	Mathematical description
No salt flow (static salt)	$v_{salt} = 0$ m·s^{-1}
Uniform temperature of 973 K throughout the 2D core model	$T = 973$ K
Six neutron energy groups	$G = 6$
Eight delayed neutron precursor groups	$I = 8$
Vacuum boundary conditions for neutron flux	$\frac{d\phi}{dx}\Big\rvert_{\text{inflow}} = 0$ m^{-2}·s^{-1}

4.1 Effective Multiplication Factor and Delayed Neutron Fraction

Moltres solves the six-group neutron diffusion equations (Equation 3.1) as a steady-state eigenvalue problem to find the k_{eff} for the static MSFR model. Table 4.2 shows the k_{eff} values from Serpent 2 and Moltres at 973 K and the corresponding salt density, and Table 4.3 shows the k_{eff} values for other temperatures at 100 K intervals. Two main factors contribute to the small discrepancies on the order of 100 pcm between the two applications: the accuracy of the neutron diffusion model, and the omission of the blanket tank structural material in Moltres. The neutron diffusion model is not as accurate as the other S_N or SP_N deterministic methods nor the Monte Carlo approach in Serpent. Regarding the omission of the blanket tank material, this model replaces the 2 cm-thick structural material with blanket salt. This replacement is partly responsible for the higher k_{eff} value calculated by Moltres as fissions occur in the blanket salt. Nevertheless, the discrepancy is smaller than the 228.5 pcm and 256.7 pcm discrepancies reported by Cervi et al. [62] for their six-group SP_3 and neutron diffusion methods, respectively.

Table 4.2: k_{eff} values from Serpent 2 and Moltres at 973 K.

Code	k_{eff}
Serpent 2	1.006 62(5)
Moltres with DNPs	1.007 940 0(10)
Moltres without DNPs	1.004 919 7(10)

Table 4.3: k_{eff} values from Serpent 2 and Moltres at various temperatures from 800 K to 1400 K.

Temperature [K]	$k_{\text{eff}} \pm \sigma$ (Serpent 2)	k_{eff} (Moltres)	Difference wrt Serpent 2 [pcm]
800	1.019 96(5)	1.021 17	121
900	1.011 72(5)	1.013 22	150
1000	1.004 28(5)	1.005 44	116
1100	0.997 35(5)	0.998 59	124
1200	0.990 06(5)	0.991 19	113
1300	0.983 56(5)	0.984 39	83
1400	0.977 02(5)	0.978 20	118

The absolute value of k_{eff} impacts the final steady-state temperature of the reactor. We can raise or lower the average core temperature at steady state to meet the design specifications for the inlet and outlet temperatures by adjusting the fissile inventory. On the other hand, the delayed neutron fraction, β, and reactivity coefficients, α, are clearer indicators of transient reactor behavior in an accident transient. β primarily affects the magnitude of the initial change in power and the time delay towards the new equilibrium power, while α affects the magnitude of the change in reactor power and temperature.

This work compares the β value from Moltres to the β_{eff} value from Serpent because Moltres currently lacks an adjoint calculation capability. The difference between β and β_{eff} is that β is the unweighted delayed neutron fraction while β_{eff} is the delayed neutron fraction weighted by the adjoint neutron flux. This work calculates β by taking the relative difference between the k_{eff} values with and without DNPs in Table 4.2. The β and β_{eff} values at 973 K, shown in Table 4.4, are in good agreement with a 4.43 pcm discrepancy.

Table 4.4: β_{eff} and β values from Serpent 2 and Moltres, respectively, at 973 K.

Code	β_{eff} [pcm]	Difference wrt Serpent [pcm]
Serpent	304.08(81)	-
Moltres	299.65(20)	4.43

4.2 Reactivity Feedback Coefficients

Temperature reactivity feedback arises mainly from Doppler broadening of resonance absorption peaks and thermal expansion. The current work reports the reactivity, ρ, values for temperatures from 800 K to 1400 K at 100 K intervals (Figure 4.1). The slopes represent the total, Doppler, density α values. The temperature range extends below the melting point of the fuel salt (841 K) to ensure that the data cover the relevant range between 841 K and 900 K. Table 4.5 shows the various α values calculated using the linear least squares approach. The total temperature coefficients from Serpent and Moltres show excellent agreement with a discrepancy of 0.019 pcm K^{-1}.

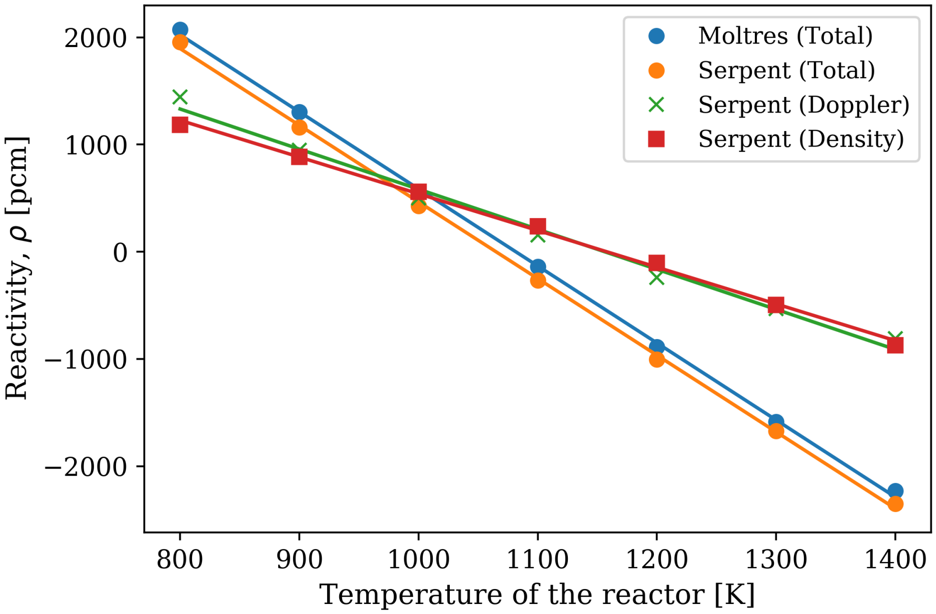

Figure 4.1: Reactivity values from Serpent and Moltres. The Doppler reactivity values were calculated at a fixed density of 4.1249 g cm^{-3}. The thermal expansion reactivity values were calculated at a fixed temperature of 973 K.

Table 4.5: Doppler, density, and total temperature coefficients for the temperature range of 800 K to 1400 K.

Software	α_D [pcm K^{-1}]	α_ρ [pcm K^{-1}]	α_T [pcm K^{-1}]
Serpent	$-3.737(13)$	$-3.424(13)$	$-7.165(13)$
Moltres	-	-	-7.184

4.3 Neutron Energy Spectrum

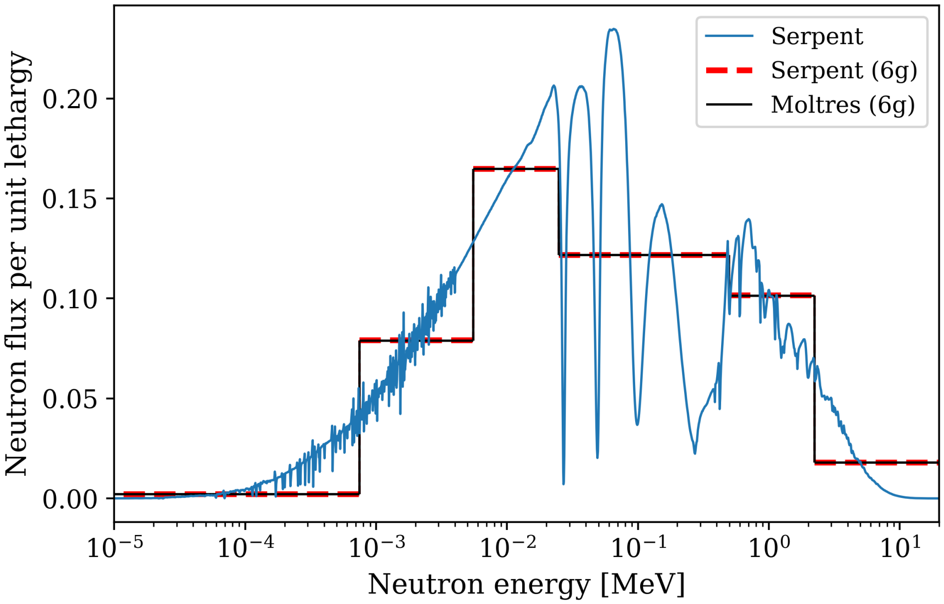

Figure 4.2: The fine-group and six-group neutron energy spectra from Serpent 2 and Moltres normalized per unit lethargy.

Moltres also closely replicated the six-group neutron spectrum from the Serpent group constants. Figure 4.2 compares the neutron energy spectra from Serpent and Moltres in the central fuel salt region. More generally, the plot shows the distinctive fast spectrum observed in the MSFR with dips in the spectrum corresponding to elastic scattering resonances from lithium and fluorine. We could obtain a more accurate representation of the neutronics in the MSFR by using more neutron energy groups with appropriate energy boundaries but this would adversely impact simulation times in the subsequent multiphysics finite element analyses.

In summary, Moltres replicated the relevant neutronics parameters accurately using the group constant data from Serpent 2. Moltres agrees with the high fidelity simulation in Serpent 2 for the

β_{eff} and temperature reactivity coefficients, which are important parameters for modeling transient reactor behavior. The k_{eff} values have discrepancies on the order of 100 pcm which are relatively small compared to other MSR multiphysics simulation tools (e.g. the neutron diffusion and SP3 models in OpenFOAM [62]).

Chapter 5

Coupled Neutronics/Thermal-Hydraulics Steady-State Results

Building on Chapter 4 which verified Moltres' neutronics modeling capabilities in the context of the MSFR, this chapter will cover the steady-state multiphysics simulation results of the MSFR using Moltres. The steady-state results depend heavily on both neutronics and thermal-hydraulics solving capabilities in Moltres. Thus, this exercise is the first verification step for Moltres as a multiphysics MSR simulation tool. This chapter will specifically discuss the temperature, velocity, neutron flux, and precursor distributions and compare them with data from the literature. The steady-state operating conditions will also serve as the initial conditions for the subsequent accident transient simulations.

This chapter will first present a summary of the procedure for obtaining the steady-state results. Next, the chapter discusses the steady-state results without modeling decay heat in direct comparison with the steady-state results from the Polimi and TUDelft models [11]. After this comparison, the chapter separately discusses the minor differences in the results from decay heat modeling in the last subsection.

5.1 Simulation Procedure

The procedure for obtaining the results for the steady-state operating conditions involved several steps due to the tightly coupled PDEs. First, a preliminary transient simulation of fluid flow in the MSFR core was run, starting from zero inlet velocity and gradually ramping up to match the nominal flow rate (4.5 $m^3\ s^{-1}$); otherwise Moltres had difficulty converging to the desired fully developed flow profile. Next, these fully developed flow values were imported as initial values for velocity in the full time-dependent simulation modeling the full coupled neutronics and thermal-hydraulics multiphysics model. The initial values for the temperature and neutron group flux distributions are 953 K and 1×10^{14} cm^{-2} s^{-1} uniformly throughout the geometry. Finally, this work assumes that model has reached steady-state when the volume integral values of every variable remain constant (up to 6 significant figures) for at least four seconds in the simulation; this period of time corresponds to the nominal circulation time of the MSFR.

5.2 Steady-State Thermal-Hydraulics Results

Figure 5.1 shows the temperature and velocity fields of the fuel salt in the core at steady-state from Moltres and the Polimi and TUDelft models. Figure 5.2 provides an alternate view of the flow profile with flow streamlines superimposed on the velocity magnitude distribution. The results from Moltres show good qualitative agreement with the Polimi and TUDelft models [10]; the plots show similar flow and hotspot features in all three models. Furthermore, the highest salt velocities in all three models occur at the inlet, outlet, and at core half-height approximately 0.40 m away from the central axis. A large recirculation region forms near the blanket tank walls. The main difference between Moltres, and the Polimi and TUDelft models is the flow profile near the central axis at the top and bottom of the core. The Polimi and TUDelft models predict relatively stagnant flow in these regions without recirculation. Moltres, on the other hand, predicts explicit recirculating flow in these regions. This is due to our constant turbulent viscosity approximation in Moltres. The k-ϵ turbulence models in the Polimi and TUDelft models predict that the turbulent viscosity in these regions is as high as 100 Pa·s, much higher than our 40 Pa·s approximation.

Nevertheless, similar temperature hotspots form in these regions of recirculation and stagnation as convection is the dominant heat transfer mechanism. The maximum temperature from Moltres, 1275 K near the bottom of the large recirculation zone, is closer to the maximum temperature in the Polimi model ($\approx$ 1300 K) than the TUDelft model ($\approx$ 1200K). Similarly, the plots show cooler temperatures in high-velocity regions. The minimum temperature is 924 K at the inlet.

Although the temperatures at the hotspots are well below the melting point of the Ni-alloy structure (1500 K), they may cause undue thermal stress on the blanket tank structure and accelerate salt corrosion rates. A sudden, large reactivity insertion could push fuel salt temperatures above the melting point of the Ni-alloy and cause irreversible damage. Furthermore, the reservoir of hot fuel salt may cause unpredictable behavior during transient scenarios when the flow profile fluctuates.

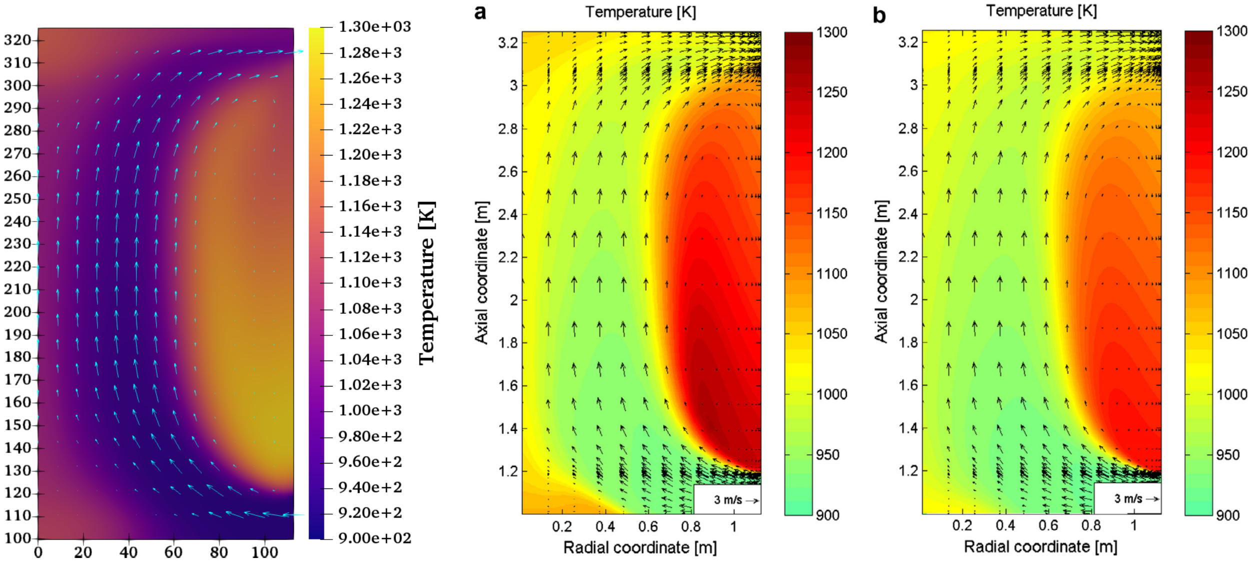

Figure 5.1: Temperature and velocity fields in the core from Moltres (left), Polimi (center), and TUDelft (right) models. The colors represent temperature according to the respective color bars and the arrows represent velocity fields.

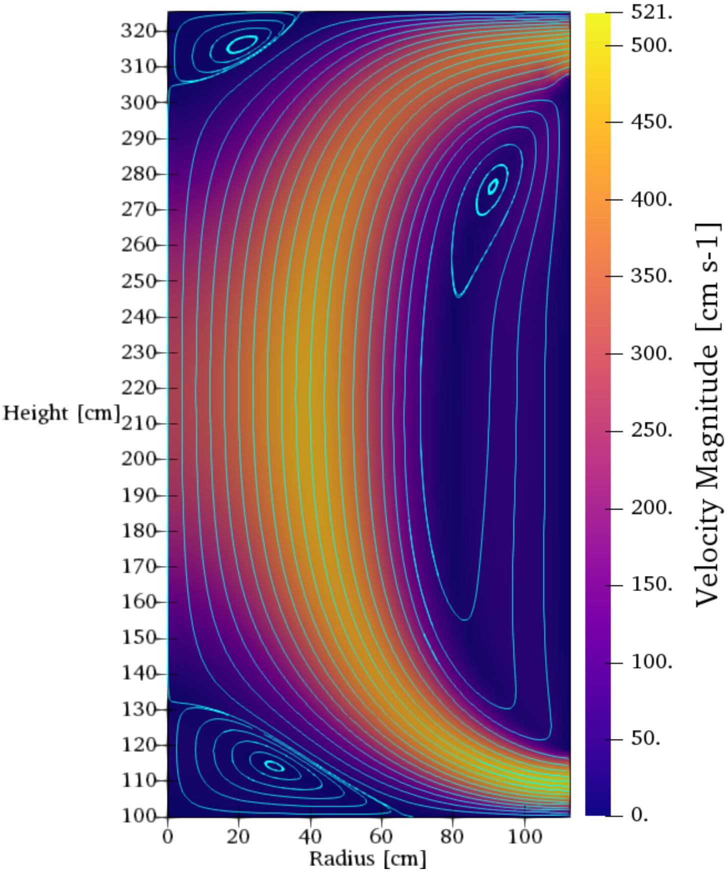

Figure 5.2: Fuel salt flow streamlines and velocity magnitude in the core from Moltres. The colors represent velocity magnitude according to the color bar on the right.

5.3 Steady-State Neutronics Results

5.3.1 Neutron Flux

The neutron flux distribution represents the heat source distribution in a nuclear reactor. Figure 5.3 shows the neutron flux distributions in the core for all six neutron energy groups, and Figure 5.4 shows the axial and radial fluxes along the center of the core and at reactor half-height, respectively. The distributions are highly symmetric along the central and horizontal axes, as expected of a cylindrical reactor design. The lower temperatures near the center of the core promote the neutron flux peaking but it is of little concern as no neutronically vulnerable structures exist in that region. The peak total flux at the center is 9.80×10^{15} $\text{cm}^{-2}\cdot\text{s}^{-1}$, which is close to values reported by Fiorina et al. [49] and Aufiero et al. [11] as shown in Table 5.1. The peak flux value from this paper is slightly higher as this work used the heterogeneous temperature distribution in Figure 5.1 while Fiorina et al. and Aufiero et al. imposed uniform temperature distributions at 973 K.

5.3.2 Delayed Neutron Fraction

As mentioned earlier, the delayed neutron precursors (DNPs) are mobile in MSRs and their distributions do not directly correspond to the neutron flux distributions. The location where the DNPs decay and emit neutrons impacts their neutron importance depending on their proximity to fissile and parasitic isotopes. Figure 5.5 shows the DNP distributions for all eight DNP groups. In general, the figures show less DNPs in the regions with fast salt flow. The precursors from the shortest-lived group (Group 8) predominantly decay within the core as their half-lives are shorter than the time it takes to reach the outlet while the precursors from the longest-lived group (Group 1) are relatively evenly distributed due to their long half-lives. For the longer-lived groups, the DNP concentrations are ill-resolved on the mesh elements adjacent to the outlet and the inlet boundaries.

Table 5.1: Peak neutron flux values from Moltres (this paper), COMSOL [49], and OpenFOAM [11] models along with the temperature distribution with which the values were obtained.

Model	Temperature distribution	Peak Neutron Flux [$\times 10^{15}$ cm^{-2} s^{-1}]
Moltres (This paper)	Steady-state	9.80
COMSOL	Uniform, 973 K	8.6
OpenFOAM	Uniform, 973 K	9.0

Thus, the present author recommends careful mesh refinement for future work involving similar geometries.

Figure 5.6 compares the total delayed neutron source distribution from Moltres with the results from the Polimi and TUDelft models [10]. In contrast to Figure 5.5 which shows the precursor distribution, Figure 5.6 shows the rate of delayed neutron emission, which was calculated by multiplying each DNP group C_i with its associated decay constant λ_i. The Polimi and TUDelft models feature greater DNP retention in the stagnant regions in the core. This effect is less pronounced in the Moltres model, most notably at the top of the core near the central axis and in the recirculation zone adjacent to the blanket tank. As mentioned in Section 5.2, only the Moltres

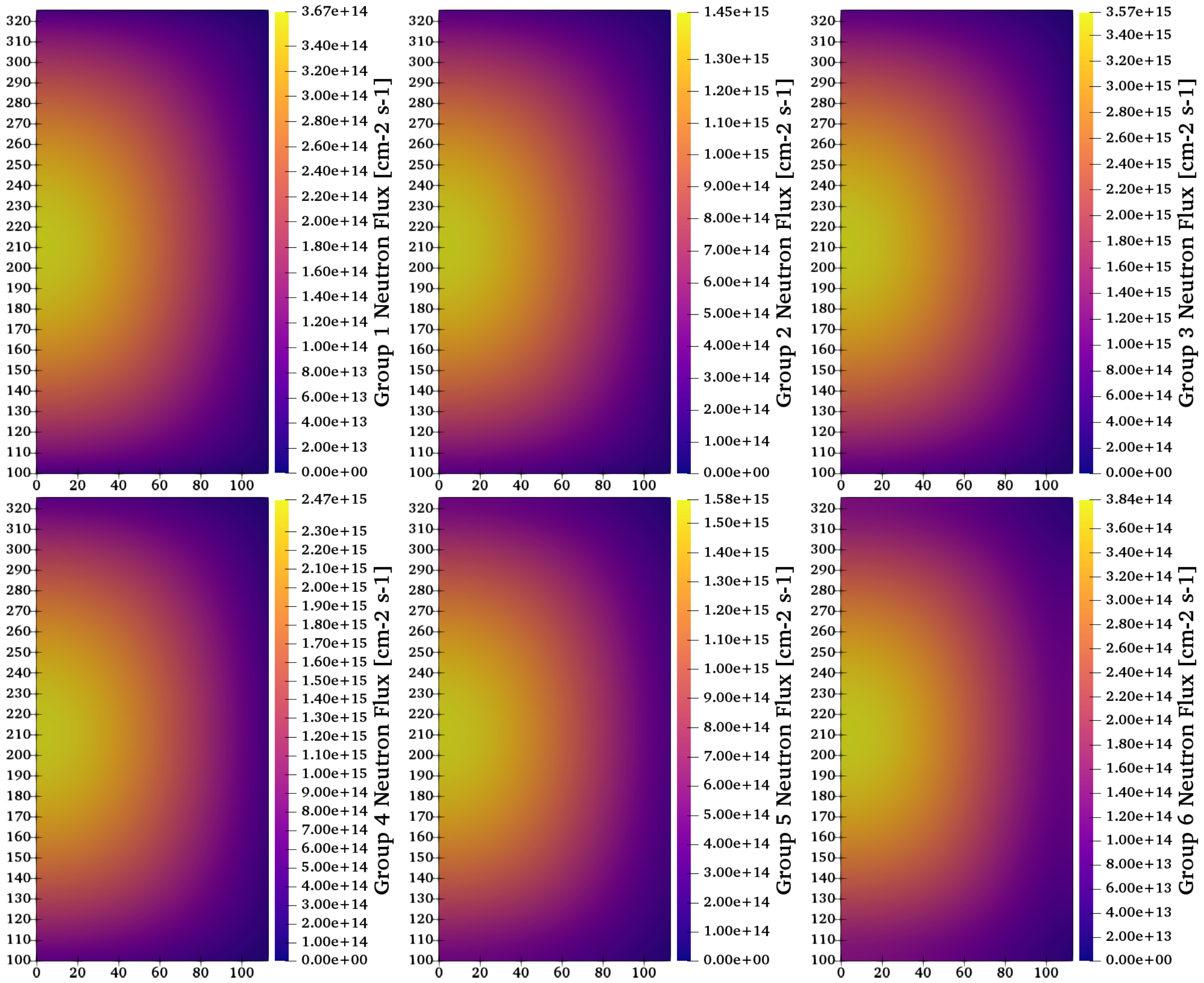

Figure 5.3: Neutron flux distributions in the core for neutron energy groups 1 to 6. The y and x axes represent height and radius (in cm) of the core relative to the entire reactor geometry. Note the different scales for each flux distribution.

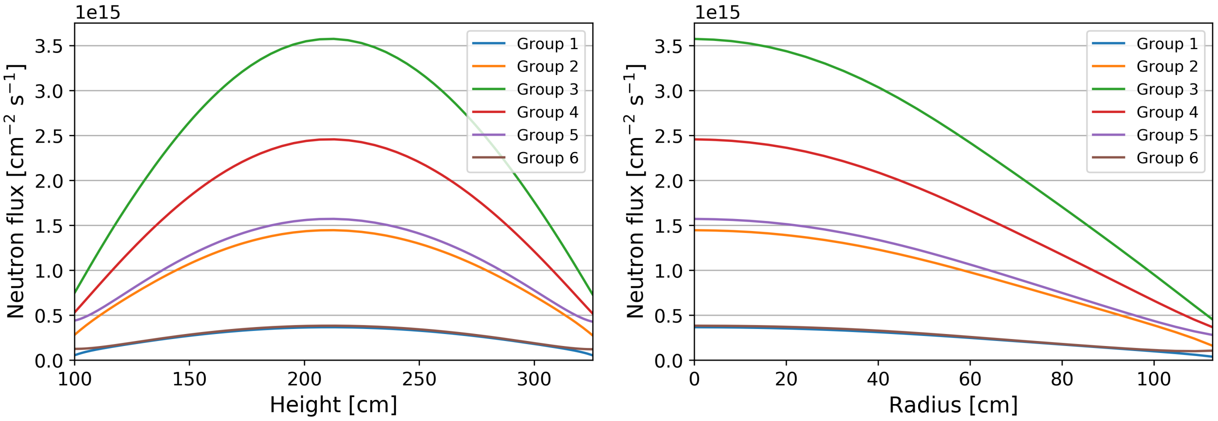

Figure 5.4: Axial (left) and radial (right) neutron flux distributions in the core for neutron energy groups 1 to 6.

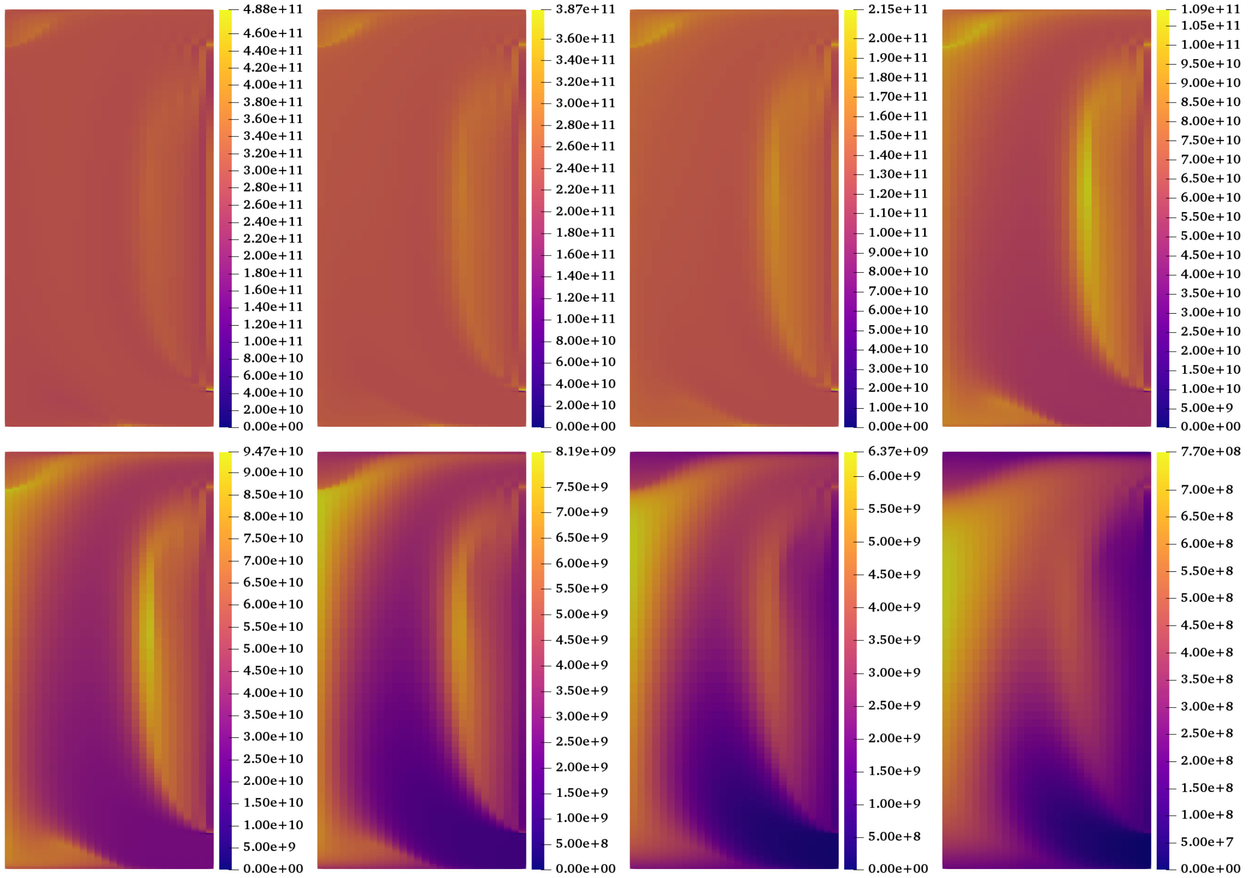

Figure 5.5: DNP distributions in the core for DNP groups 1 to 8 (from left to right, top to bottom). Refer to Figure 5.3 for the height and radius scales on the y and x axes, respectively. Note the different scales for each distribution.

model features a small recirculation zone at the top of the core. This local flow pattern is responsible for diverting the shorter-lived DNPs away from the top of the core and reducing the build-up in that region.

The in-core delayed neutron fraction, which we denote as β_c, is an important safety parameter for MSRs. This value represents the actual delayed neutron fraction in MSRs after accounting for the loss of delayed neutrons from DNPs decaying outside the active core region. Reactors with smaller β values exhibit greater prompt jumps in the neutron flux in response to reactivity insertions because they have a greater proportion of prompt neutrons under normal operating conditions. This effect is undesirable from a reactor safety perspective because it reduces the time available for active safety mechanisms to activate and scram the reactor. In MSRs, the strong, negative fuel temperature reactivity coefficient partly mitigates the sharp increase in neutron flux. Chapter 6 contains more in-depth discussions for various transient scenarios.

Table 5.2 compares the fraction of out-of-core emissions and the β_c values from Moltres with the Polimi and TUDelft models. The present author calculated the fraction of out-of-core emissions by finding the average concentration of each DNP group in the core and the outer loop, multiplying each average by their associated decay time constants λ_i for the average emission rate, and calculating the

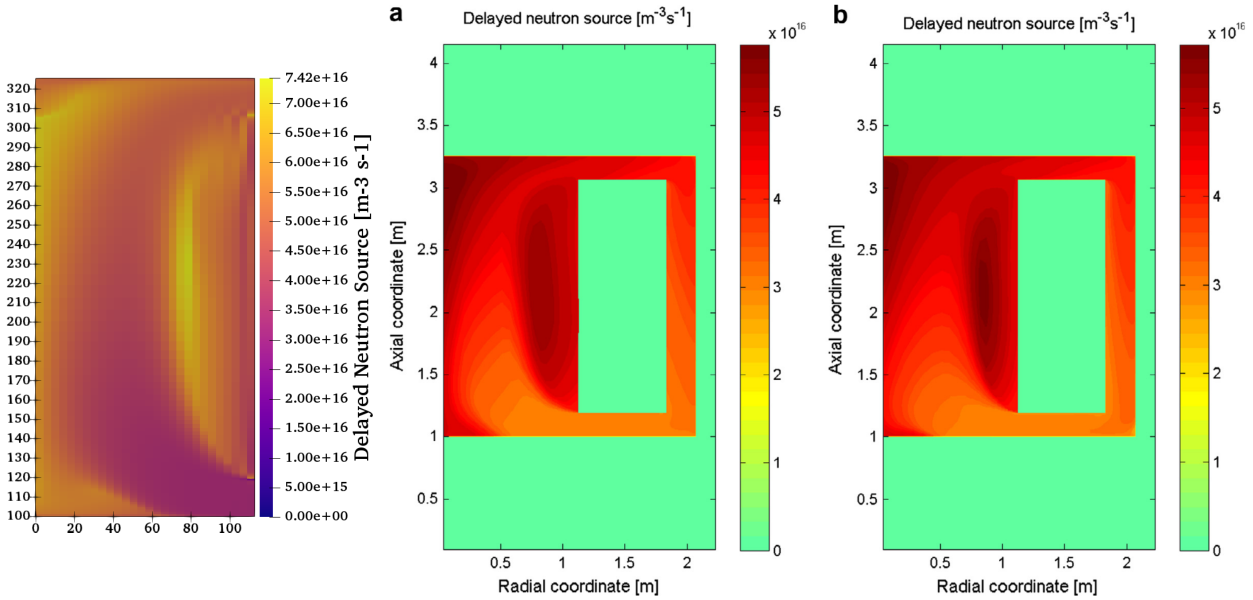

Figure 5.6: Total delayed neutron source distribution in the core from Moltres (left), Polimi (center), and TUDelft (right) models.

Table 5.2: The fraction of delayed neutrons lost from out-of-core emission and the in-core delayed neutron fraction β_c values from Moltres (this paper), and the Polimi and TUDelft models [10].

Model	Out-of-Core Emission [%]	β_c [pcm]
Moltres (This paper)	44.16	184.9
Polimi	34.80	134.3
TUDelft	34.85	123.8

proportion of emissions in the outer loop relative to the total sum. The present author calculated β_c by first obtaining the prompt neutron emission rate from Moltres and subsequently using the in-core delayed neutron emission rate from the previous calculation to find the fraction of delayed neutron emission rate relative to total emission rate.

The fraction of out-of-core emissions from the Moltres model differs significantly by approximately 10%, and β_c differs by 60-70 pcm. The former is attributed to the lesser DNP retention in the stagnant flow regions in the core; the DNPs are more evenly distributed along the entire primary loop and a greater fraction of delayed neutron emissions occur in the outer loop region. The flow patterns are responsible for the distribution of shorter-lived DNP since convection is the dominant mode of species transport in the MSFR. The exact flow pattern in the recirculation zones in the Polimi and TUDelft models differs from that in Moltres (Figure 5.2). Figure 5.1 also shows some minor differences in the magnitude of the flow in the recirculation zones between Moltres, and the Polimi and TUDelft models. Although the sizes of the arrows representing flow velocity are on different scales, a quick comparison between the largest arrows and the arrows in the recirculation zone indicates that the recirculation zone in Moltres is more stagnant. This could explain the concentration of DNPs along an “arc” closer to the center of the core in Moltres as opposed to the more even distribution of DNPs throughout the whole recirculation zones in the Polimi and TUDelft models. The higher peak DNP distribution in Moltres also supports this assertion.

In spite of the greater delayed neutron losses, the β_c value is higher in Moltres than the Polimi and TUDelft models. Fiorina et al. [10] applied adjoint flux weighting for their β_c calculation whereas this work reports the value as the physical fraction without adjoint weighting. The adjoint weighting results in a smaller β_c because a greater fraction of the DNPs decay in the recirculation zones, where the neutron importance is noticeably diminished. Fast reactors also typically have smaller β_{eff} because the fission cross sections of fertile isotopes (e.g. ^{238}U and ^{232}Th) monotonically decrease with decreasing neutron energy [63]. On average, delayed neutrons are less energetic than prompt neutrons.

5.4 Steady-State Decay Heat Results

The movement of decay heat precursors effectively redistributes a fraction of the fission heat source concentrated at the center of the core to other parts of the primary loop. Thus, the temperature distribution in the core should show less extreme temperatures compared with the simulation without decay heat.

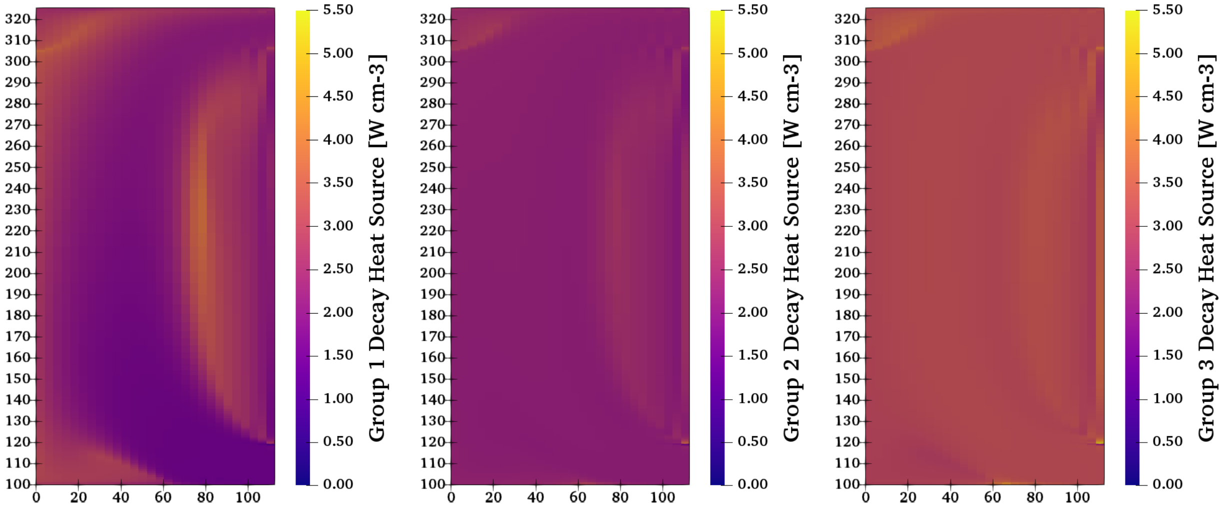

Figure 5.7: Decay heat source distribution in the core for decay heat groups 1 to 3 (from left to right). Refer to Figure 5.8 for the height and radius scales on the y and x axes, respectively. Note the different scales for each distribution.

Figure 5.7 shows the decay heat source distribution in the core for groups 1 to 3. Readers may refer to Table 3.2 for the associated decay time constants. Similar to the delayed neutron precursor distributions, the shorter-lived decay heat precursors show greater build-up in the recirculation zones compared with the longer-lived decay heat precursors that are more evenly distributed throughout the core.

Figure 5.8 shows the difference in core temperatures at steady-state with decay heat modeling relative to the core temperatures without decay heat in Figure 5.1. This figure uses a different color map to clearly distinguish between positive and negative temperature differences in the core. The hotspots in the recirculation zones are approximately 2 to 4 K cooler, while the cooled salt flowing in from the inlet is approximately 2 K hotter. These regions correspond to the hottest and coldest areas in the core and the results agree with the expectation that the extreme temperatures would be affected the most by the introduction of decay heat precursors. The difference between the outlet and inlet temperatures falls from 101.1 K to 98.9 K as some of the decay heat precursors deposit heat in the outer loop region. The figure also shows some nonphysical oscillations in the temperature near the outlet because the mesh near the boundary is too coarse for the given outlet velocities. Users can avoid these oscillations near the outlet by using a mesh that is progressively finer towards the boundary. This exercise is left as an objective for future work.

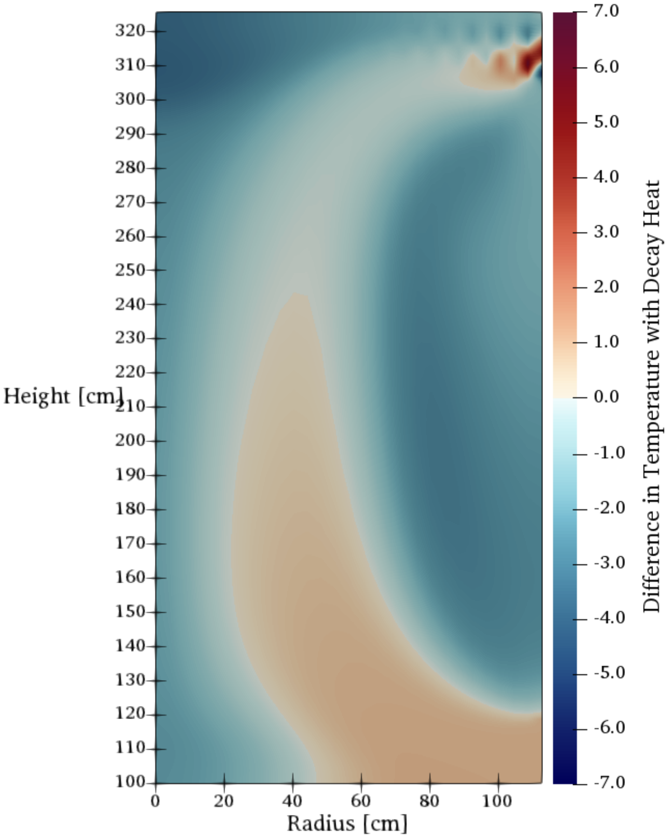

Figure 5.8: Difference in core temperatures at steady-state with decay heat relative to the result without decay heat (Figure 5.1).

Chapter 6

Transient Scenarios

This chapter discusses Moltres transient multiphysics simulations of the MSFR in four accident scenarios. These scenarios, adapted from the MSFR transient analyses with the Polimi and TUDelft models [10], include unprotected reactivity insertion, loss of heat sink, loss of flow, and pump overspeed accidents. The term “unprotected” signifies accident scenarios without reactor SCRAM. As such, these simulations provide an insight on the MSFR’s passive safety capabilities in the absence of active safety systems. This work used the steady-state configuration presented in the previous chapter as the initial conditions for the transient simulations discussed in this chapter. Specifically, all steady-state spatial values for neutron flux, delayed neutron precursor concentration, temperature, velocity, and pressure were imported as the initial state of the transient scenarios.

As noted by Fiorina et al. [10], explicit decay heat modeling has a negligible effect in reactivity-, and pump-initiated transients. Furthermore, only their Polimi model had this capability. Therefore, they included decay heat modeling for the loss of heat sink accident scenario only. The current work also ran all transient simulations without the decay heat model for a fair comparison. The only exception is the loss of heat sink scenario in which two separate simulations with and without the decay heat model were run. This work imposed simplifying assumptions in our transient models to match the implementations in [10] as closely as possible, within Moltres’ capabilities. The details of the setup for each transient simulation appear in the following sections.

6.1 Unprotected Reactivity Insertion

In reactivity insertion accidents, excess reactivity would drive an increase in flux, power, and temperature. In MSRs, a positive reactivity insertion could occur if the online refueling system injected excess fissile material into the core. Excessively high neutron fluences and temperatures could negatively impact reactor structural integrity and increase the risk of containment breach.

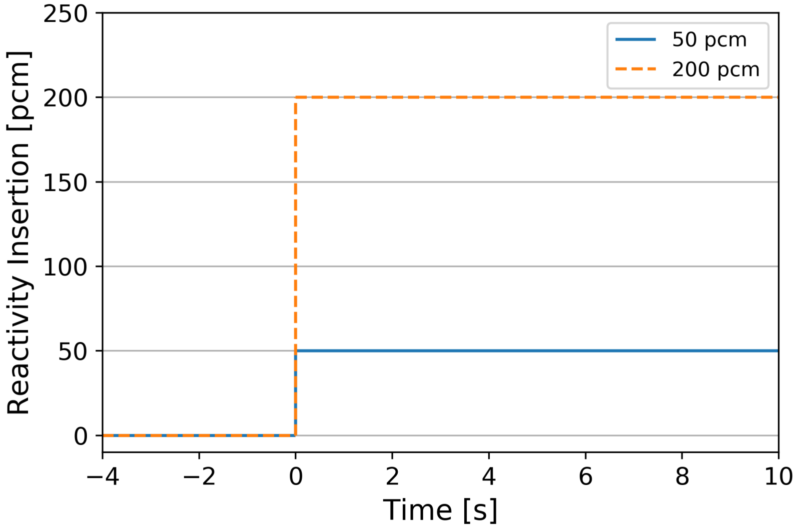

Figure 6.1: Step-wise 50 pcm and 200 pcm reactivity insertions used to initiate the accident transients.

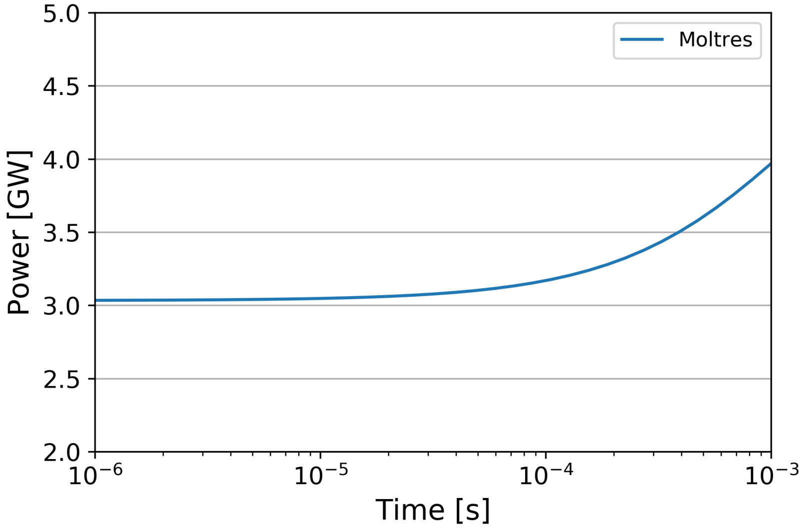

Figure 6.2: Power output during the prompt response following a 50 pcm step-wise unprotected reactivity insertion in the Moltres model.

This work modeled two unprotected step-wise reactivity insertion scenarios in Moltres by swapping out the original set of group constant data with two new, separate sets of data from Serpent corresponding to 50 pcm and 200 pcm reactivity insertions, respectively. The reactivity of the Serpent MSFR models was increased by increasing the ^{233}U-to-^{232}Th ratio in the fuel salt. Figure 6.1 shows the step-wise reactivity insertions used to model the accident scenarios.

The neutronic and thermal-hydraulic behaviors of the reactor core are the focus of this transient study. Thus, this work assumes that the heat exchanger and the associated power generation equipment (generator turbines, heat sinks, etc.) can withstand all variations in the power output during the transients.

Figure 6.2 shows the rise in power output during the initial prompt response. The prompt response raises the power output to 4 GW by $t = 0.001$ s. Figures 6.3 and 6.4 show the power output and average core temperature increase beyond $t = 0.001$ s following the 50 pcm step-wise reactivity insertion in the Moltres, Polimi, and TUDelft models. Power continues to rise at a slower rate up to 4.63 GW at around $t = 0.005$ s, at which point the negative reactivity from the Doppler effect and salt expansion becomes greater than the initial +50 pcm insertion. Power continues to fall as the average core temperature rises. A slight change in slope occurs at $t = 0.3$ s. The elapsed time approximately corresponds to the average half-life of the two shortest-lived delayed neutron precursor (DNP) groups ($t_{1/2} = 0.195$ s and 0.424 s); the decay of the surplus precursors produced in the initial phase negates a fraction of the negative reactivity from the elevated core temperature. By $t = 3$ s, most of the heated salt and DNPs from the initial phase will have circulated the primary loop and returned to the core. The heated salt causes a small, noticeable dip in power before the power output stabilizes.

The average core temperature rises steadily from the start of the transient until $t = 3$ s when the heated salt from the initial phase returns to the core. This event is characterized by the small peak in the average core temperature at $t = 3$ s. The subsequent drop in power output halts the temperature increase and the core tends to a new equilibrium average temperature approximately 7.5 K higher than the initial average temperature.

The results from Moltres show good agreement with the results from the Polimi and TUDelft models; Moltres reproduced all of the individual features in both plots. The magnitude of the reactor response is the most significant difference. Moltres predicts a smaller peak in the power output and a smaller overall increase in the average core temperature mainly due to the more negative temperature reactivity coefficient in Moltres than in the Polimi and TUDelft models. The

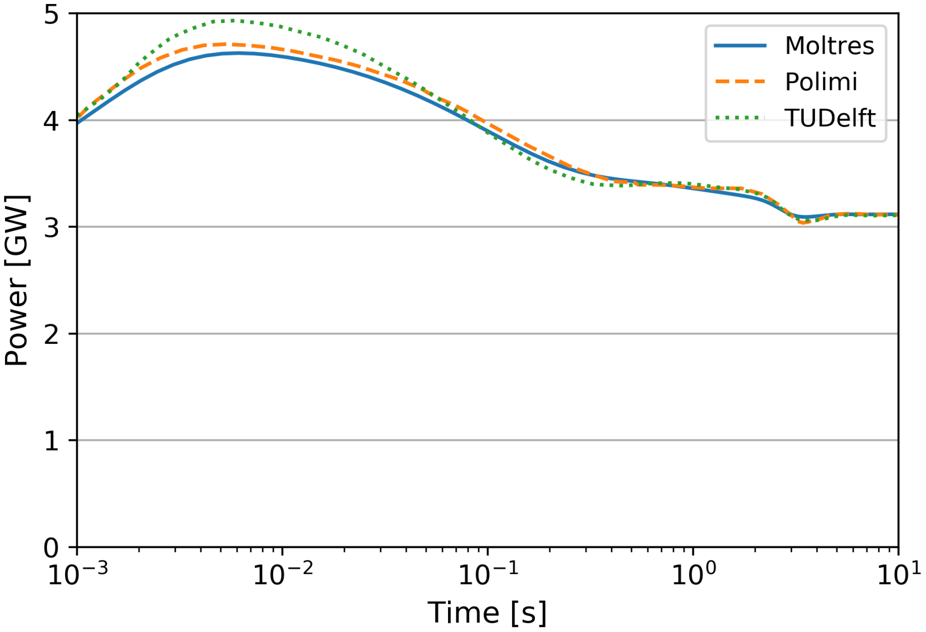

Figure 6.3: Power output following a 50 pcm step-wise unprotected reactivity insertion in the Moltres, Polimi, and TUDelft models [10].

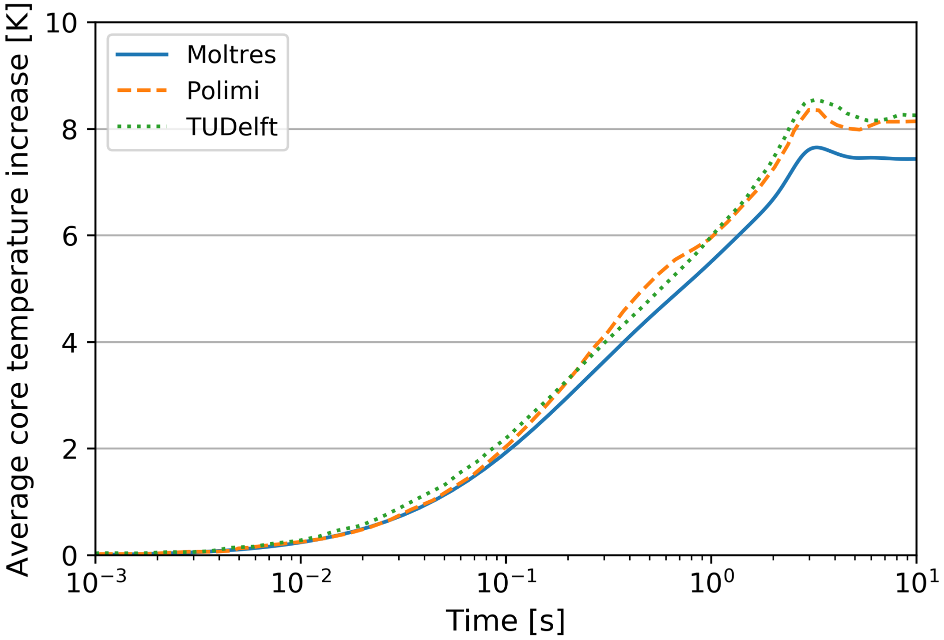

Figure 6.4: Average core temperature increase following a 50 pcm step-wise unprotected reactivity insertion in the Moltres, Polimi, and TUDelft models [10].

temperature reactivity coefficient α_T in Moltres is -7.184 pcm K^{-1} (Table 4.5), as opposed to approximately -6.5 pcm K^{-1} within the relevant temperature range in the Polimi and TUDelft models. Therefore, the results show a smaller temperature increase in the Moltres model for the same reactivity insertion. Multiplying the average core temperature increase at $t = 10$ s with α_T gives us -7.184 pcm $\text{K}^{-1} \times 7.46$ K $= -53.6$ pcm, which is approximately equal to the 50 pcm reactivity insertion.

The results for the 200 pcm reactivity insertion scenario show similar trends to the 50 pcm case. The greater reactivity insertion elicits a stronger prompt response in the power output which peaks at 92.1 GW. The average core temperature increases much more rapidly and subsequently triggers a sharper drop in power output. This more clearly distinguishes the rate of core temperature increase before and after $t = 0.01$ s. The difference in α_T causes greater deviations in the results between Moltres and the other models. Overall, Moltres' results show good agreement with the Polimi and TUDelft results. The differences arise mainly due to the differences in the temperature reactivity coefficients.

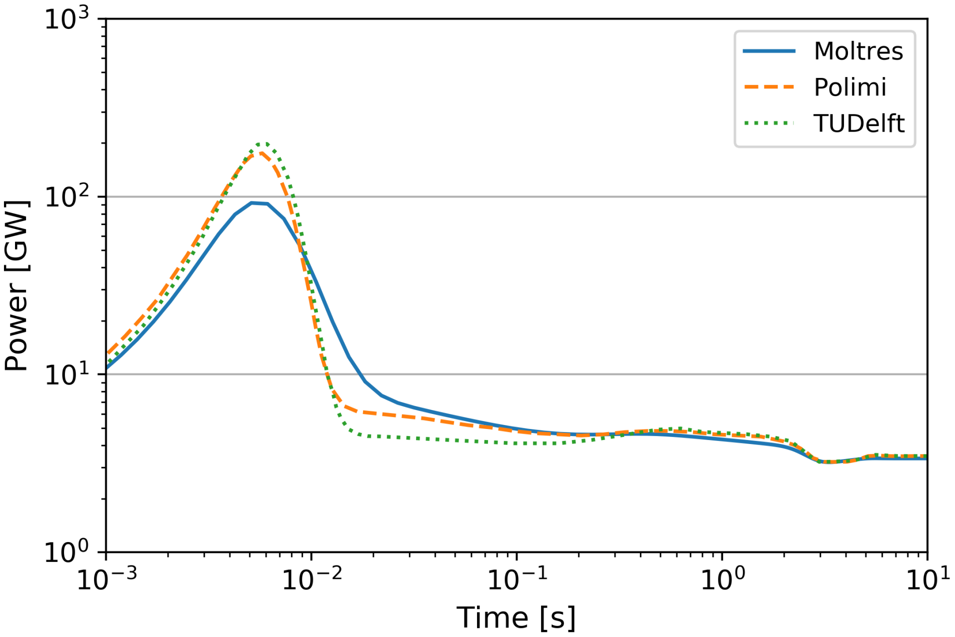

Figure 6.5: Power output following a 200 pcm step-wise unprotected reactivity insertion in the Moltres, Polimi, and TUDelft models [10].

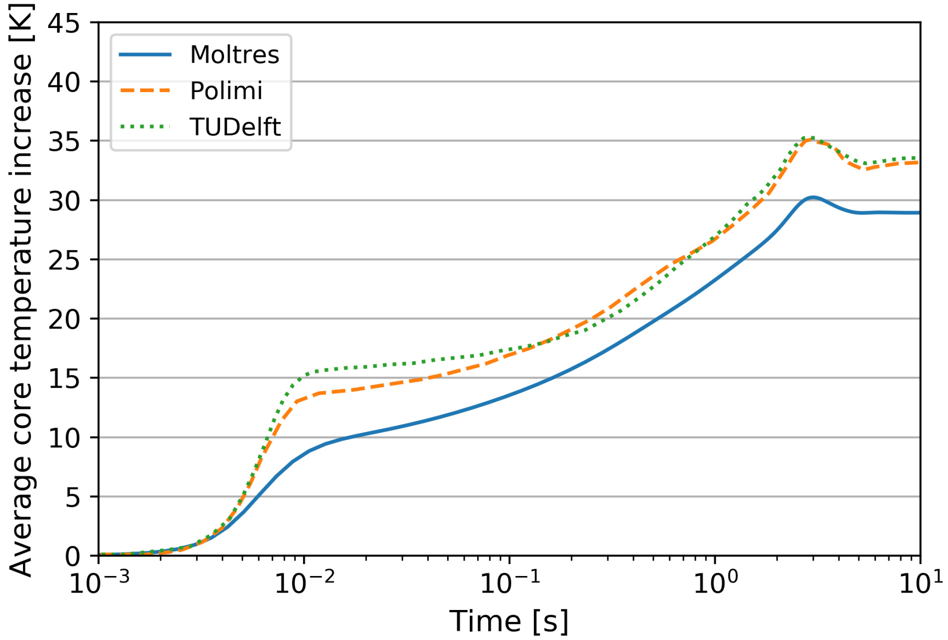

Figure 6.6: Average core temperature increase following a 200 pcm step-wise unprotected reactivity insertion in the Moltres, Polimi, and TUDelft models [10].

6.2 Unprotected Loss of Heat Sink

An unprotected loss of heat sink accident can occur when the pumps in the intermediate loop fail and reactor is not SCRAMed. The heat exchangers would then lose most of their cooling capabilities. This work followed Fiorina et al.'s approach in assuming that the cooling from the heat exchangers decreases exponentially with a time constant of 1 s and all other parameters held constant [10]. As mentioned in the Chapter 5, we will present two sets of results for this transient: 1) without decay heat modeling, and 2) with decay heat modeling.

6.2.1 Without Decay Heat

Figures 6.7 and 6.8 show the power output and average core temperature increase during the unprotected loss of heat sink transient in the Moltres, Polimi, and TUDelft models without decay heat modeling. The power output and average core temperature show little change in the first two seconds as it takes approximately that amount of time for the partially cooled salt to migrate to the center of the core. At $t = 2$ s, we observe a sharp spike in average core temperature and a corresponding drop in power output. The presence of delayed neutron precursors (DNPs) from the steady-state operating conditions momentarily halt the increase in temperature at around $t = 5$ s. The average core temperature continues to rise while the power output falls through the rest of the transient.

The results from Moltres show good agreement with the results from the Polimi and TUDelft. Moltres reproduced all of the trends in the Polimi and TUDelft models. The temporary halt in the temperature increase occurs at a lower average core temperature for Moltres than the other two models. This is likely due to the difference in the temperature reactivity coefficient discussed in the reactivity insertion results; a smaller increase in the average core temperature produces the same decrease in power output.

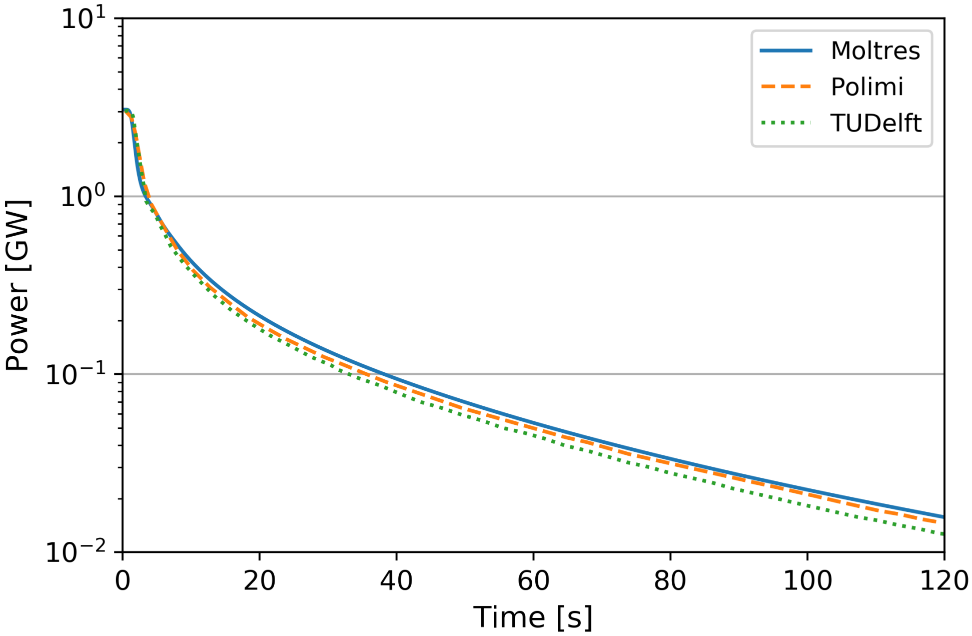

Figure 6.7: Power output during an unprotected loss of heat sink transient in the Moltres, Polimi, and TUDelft models [10] without decay heat.

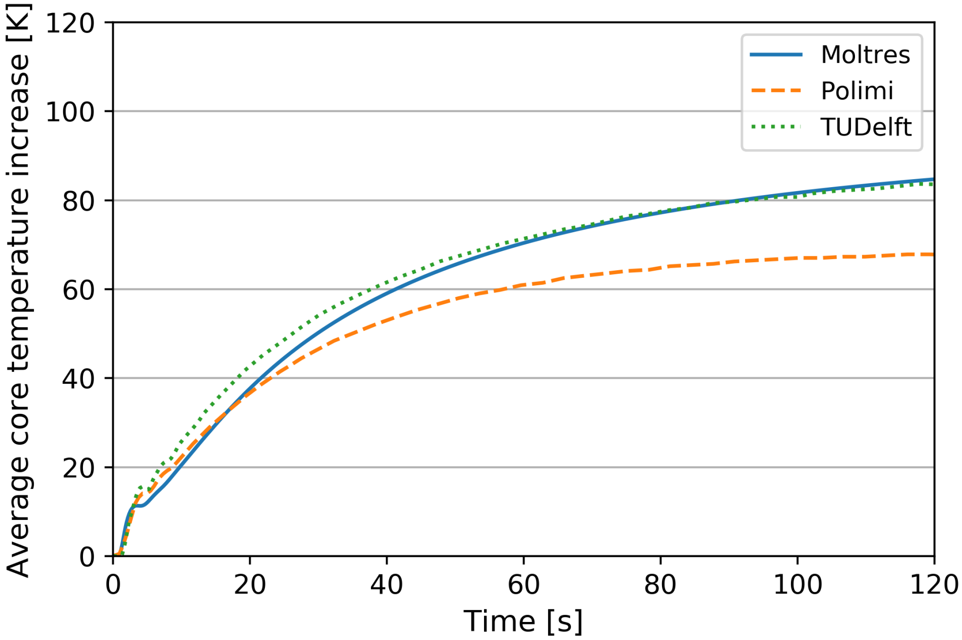

Figure 6.8: Average core temperature increase during an unprotected loss of heat sink transient in the Moltres, Polimi, and TUDelft models [10] without decay heat.

6.2.2 With Decay Heat

Decay heat from fission products poses a great safety risk in an unprotected loss of heat sink accident. Section 6.2.1 showed that prompt fission power output quickly falls as core temperatures rise. However, decay power output is independent of the instantaneous neutron flux. Figure 6.9 shows that the decay power output remains relatively high during a short-term transient. Decay heat becomes the dominant heat source from $t = 34$ s and falls at a much slower rate than prompt heat. Figure 6.10 highlights the greater core temperature increase arising from decay heat as compared with the results without decay heat. By $t = 120$ s, the model with decay heat records an average core temperature increase that is 45 K higher than the model without decay heat. The absolute core temperature reaches approximately 1220 K and would continue to rise further. This places undue thermal stress and accelerates salt-induced corrosion in the Hastelloy structural material. In the absence of an auxiliary heat removal system in the primary loop, reactor operators would have to rely on the freeze plug to drain the core into a drain tank with emergency cooling systems to keep the salt cool.

Figure 6.11 shows the loop-averaged temperature increase in the Moltres and Polimi models [10]. The TUDelft model does not have a decay heat modeling capability. The Moltres model predicts the same increasing trend in the temperature. The loop-averaged temperature rises significantly at the start of the transient and continues to rise at a decreasing rate. The loop-averaged temperature increase in the Moltres model at $t = 120$ s is approximately 17 K lower than that in the Polimi model. Unfortunately, the power profile from the Polimi model is not available for direct comparison. However, if the decay power output were similar, the stronger negative temperature reactivity coefficient would cause the prompt power output in the Moltres model to fall faster than the Polimi model. Consequently, the loop-averaged temperature would be lower as shown in the figure. Overall, the results for the loss of heat sink transient agree with the Polimi and TUDelft model results in both cases, with and without decay heat modeling.

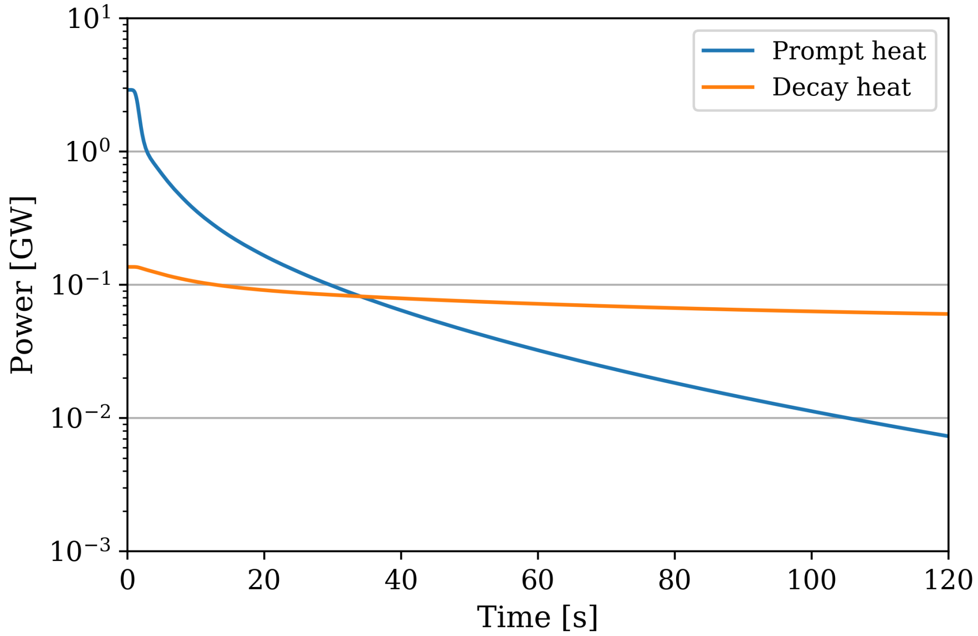

Figure 6.9: Power output during an unprotected loss of heat sink transient in the Moltres model with decay heat.

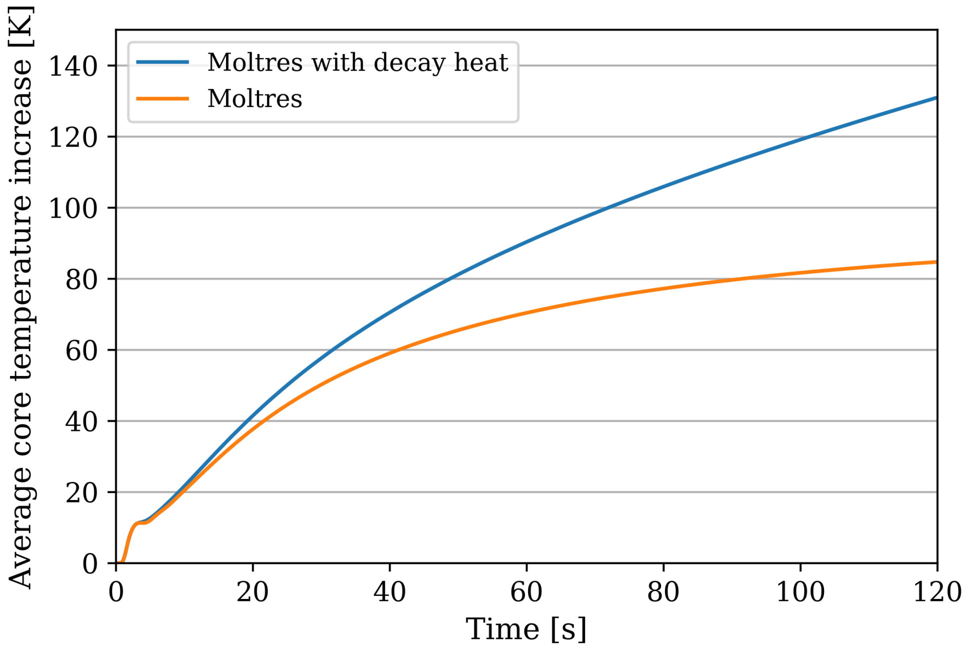

Figure 6.10: Average core temperature increase during an unprotected loss of heat sink transient in the Moltres model with and without decay heat.

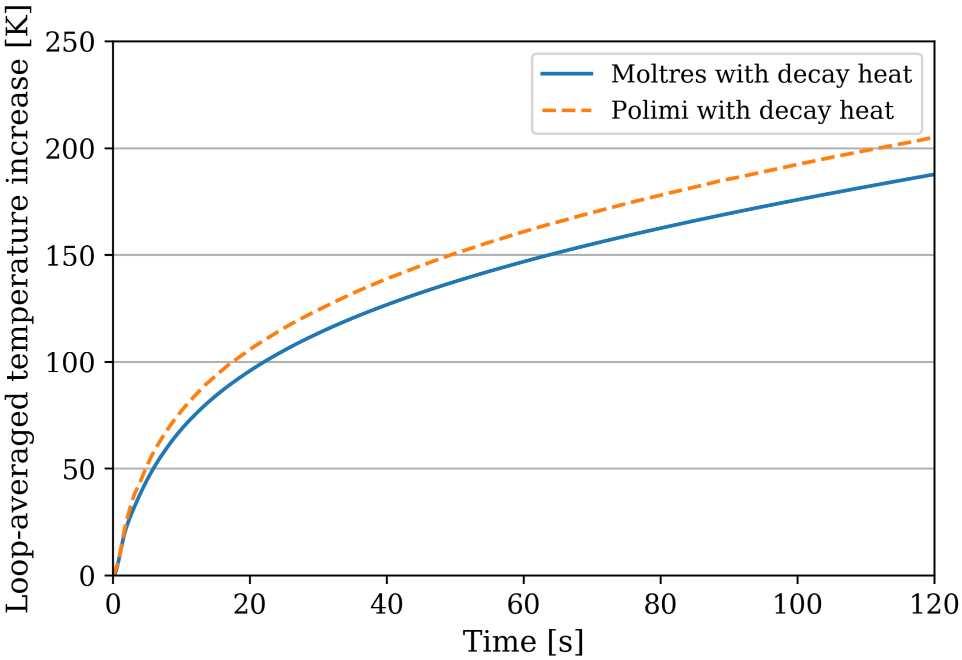

Figure 6.11: Loop-averaged temperature increase during an unprotected loss of heat sink transient in the Moltres and Polimi models [10] with decay heat.

6.3 Unprotected Pump Overspeed

Pump overspeed refers to a sustained increase in pump speed in the primary coolant loop. The increased flow rate $\dot{V}$ impacts reactor performance in several ways. It reduces the in-core β as more of the shorter-lived precursors will tend to flow out of the core and decay in the subcritical outer loop region. The increased $\dot{V}$ also enhances the heat transfer coefficient on the primary loop side of the heat exchanger and introduces cooler fuel salt to the core. The reactivity increase from the temperature reactivity feedback outweighs the reactivity decrease from the loss of delayed neutrons. Thus, the overall neutron flux and power output is higher at the new equilibrium state. At the same time, the improved mixing flattens the temperature distribution in the core.

This work followed the Polimi and TUDelft models [10] by ramping up the inlet velocity, u, by 50% from the nominal value, u_0, according to the following formula:

$$u(t) = u_0[1 + 0.5(1 - e^{-t/\tau})] \tag{6.1}$$

where

$$\tau = 5 \text{ s}.$$

For this transient, this work assumed that μ_t was directly proportional to v because the buoyancy effects are assumed to be negligible with forced flow and the recirculation zones persist throughout the entire duration.

Setting the exact dependence between the heat transfer coefficient h and $\dot{V}$ was problematic because the pointwise heat exchanger implementation in Moltres performs differently compared with the heat exchangers of finite volume in the Polimi and TUDelft models [10]. In a heat exchanger of finite volume, most of the cooling occurs in the first half of the heat exchanger where the temperature differential between the primary and intermediate loops is the largest. In the Polimi and TUDelft models, the overall h is a harmonic mean of the h_i on each side of the heat exchanger, given as:

$$h = \frac{2}{\frac{1}{h_1} + \frac{1}{h_2}}, \tag{6.2}$$

where

$$\begin{aligned} h &= \text{overall heat transfer coefficient } [\text{W}\cdot\text{K}^{-1}], \\ h_1 &= \text{heat transfer coefficient on the primary loop side } [\text{W}\cdot\text{K}^{-1}], \\ h_2 &= \text{heat transfer coefficient on the intermediate loop side } [\text{W}\cdot\text{K}^{-1}]. \end{aligned}$$

In addition to this, the Polimi and TUDelft models used the Dittus-Boelter correlation [64] for the relationship between h_1 and $\dot{V}$. The Dittus-Boelter correlation for fluids being cooled is:

$$Nu = 0.023 Re^{0.8} Pr^{0.3}, \tag{6.3}$$

where

$$Nu = \text{Nusselt number} = \frac{\text{convective heat transfer}}{\text{conductive heat transfer}} = \frac{hL}{k},$$

$$
\begin{aligned}
Re &= \text{Reynolds number} = \frac{\text{inertial forces}}{\text{viscous forces}} = \frac{\rho u L}{\mu}, \\
Pr &= \text{Prandtl number} = \frac{\text{momentum diffusivity}}{\text{thermal diffusivity}} = \frac{c_p \mu}{k}.
\end{aligned}
$$

The only direct relation to $\dot{V}$ in the Dittus-Boelter correlation is through the Reynolds number, Re, which is directly proportional to flow velocity v. This gives the following relation between h and v:

$$
\begin{aligned}
& h \propto v^{0.8} \qquad (6.4) \\
& h = \text{heat transfer coefficient } [\text{W}\cdot\text{K}^{-1}], \\
& v = \text{flow velocity } [\text{m}\cdot\text{s}^{-1}].
\end{aligned}
$$

However, this relation provided very different results in the unprotected pump overspeed and loss of flow transients compared with the Polimi and TUDelft models. This approach underpredicted the equilibrium power output in the unprotected pump overspeed transient and overpredicted the same parameter in the unprotected loss of flow transient. Upon further investigation, it was found that raising the power of v from 0.8 to 1.1 brought the average core temperatures closer to the results from the other models in both transients. Therefore, this work adopted the raised power in this thesis.

Figures 6.12 and 6.13 show the power output and average core temperature increase during the unprotected pump overspeed transient in the Moltres, Polimi, and TUDelft models. Figure 6.14 shows the same results for the first 20 seconds of the transient. At the start of the transient, the rising flow rate cools the core by convecting heat away from the center and causes power output to rise sharply. Although the average core temperature has a strictly decreasing trend, the temperature at the center of the core briefly rises due to the sharp increase in power output. Since this is the region where most of the fissions take place, the Doppler effect and salt expansion causes the power output to stall and dip briefly before rising again at $t = 2.5$ s. The reactor tends to a new equilibrium power output and average core temperature. The temperature distribution in the core is more evenly distributed because the turbulent thermal conductivity k_t is directly proportional to μ_t.

In both sets of results, Moltres reproduced all of the transient features found in the Polimi and

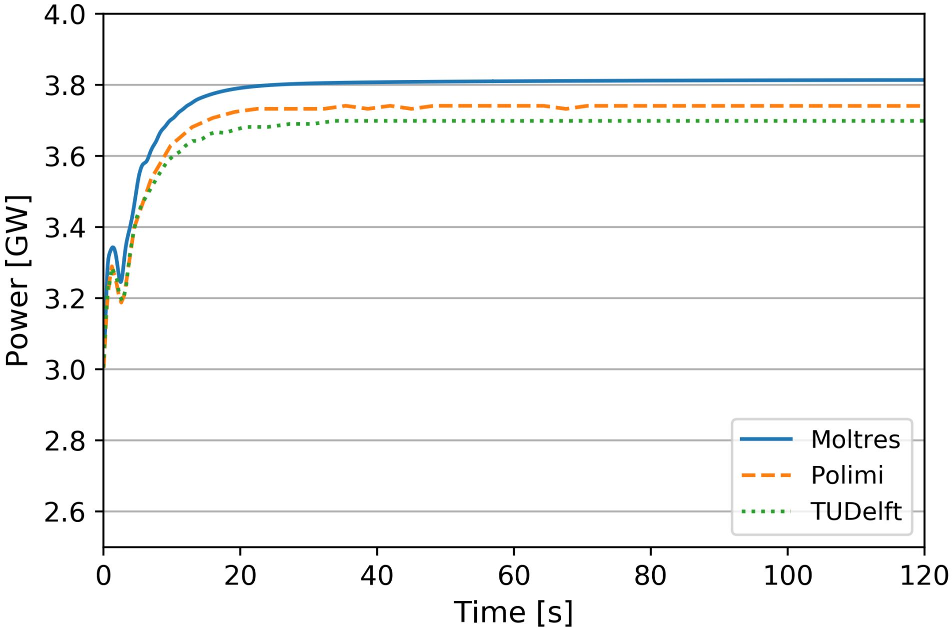

Figure 6.12: Power output during an unprotected pump overspeed transient in the Moltres, Polimi, and TUDelft models [10].

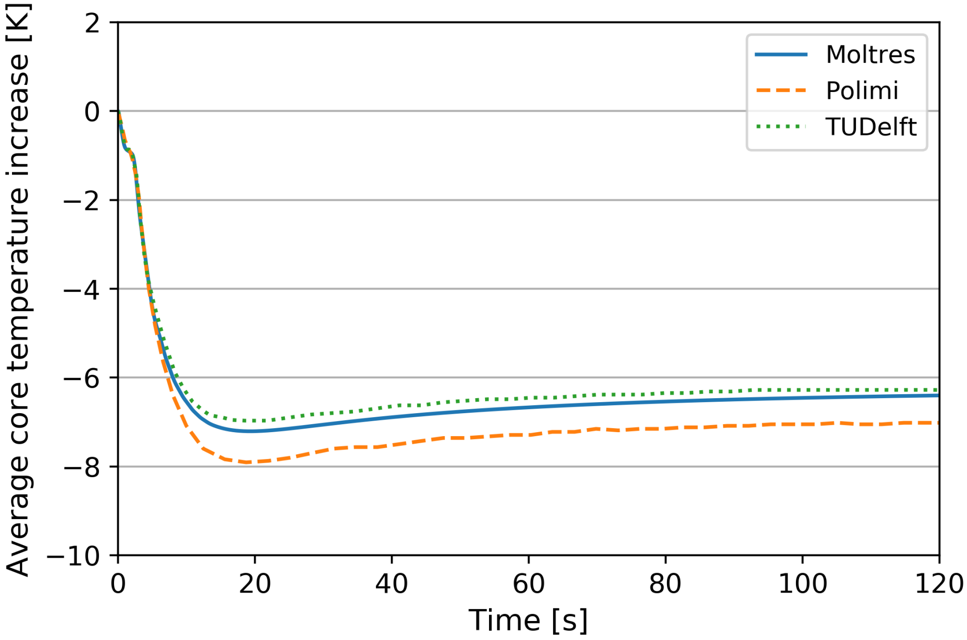

Figure 6.13: Average core temperature increase during an unprotected pump overspeed transient in the Moltres, Polimi, and TUDelft models [10].

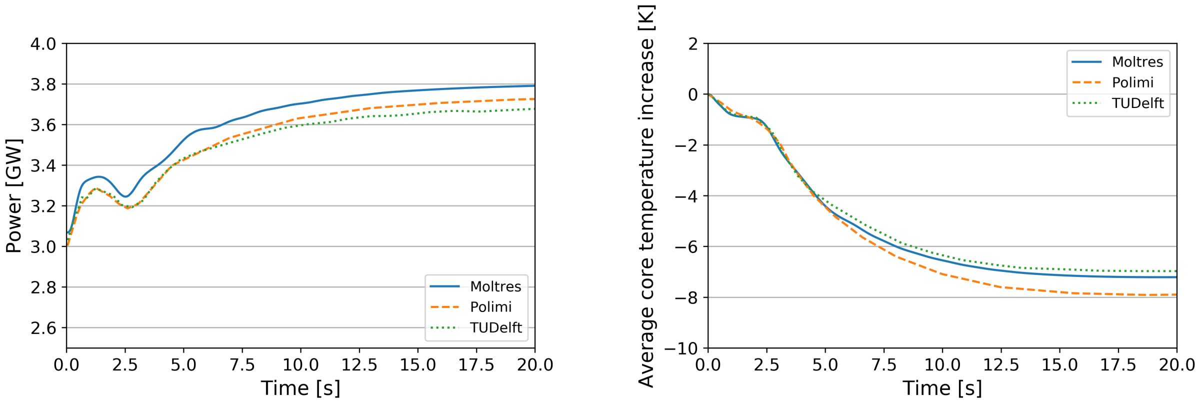

Figure 6.14: The first 20 s of the power output and average core temperature increase during an unprotected pump overspeed transient.

TUDelft models. The average core temperature profile falls between the Polimi and TUDelft results, while the power output is approximately 0.1 GW higher because the Moltres MSFR model has a greater α_T than the other two models.

6.4 Unprotected Loss of Flow

A loss of forced flow transient can occur in the event of a station blackout without reactor SCRAM; the pumps would cease operating due to the loss of AC electrical power. Natural circulation resulting from temperature-dependent density changes becomes the dominant driving force for salt flow in the primary loop. Fiorina et al. [10] applied the Boussinesq approximation for buoyancy-driven flow in the Polimi and TUDelft models, but this approach was not possible in Moltres because the primary loop is partitioned into two separate geometries and uses Dirichlet boundary conditions at the inlet to drive flow. The Polimi and TUDelft models featured complete exponential coast-downs of the pumps with a time constant of 5 s. The final flow rate $\dot{V}_f$ from natural circulation was approximately 18 times smaller than the initial $\dot{V}_0$. Figure 6.15 shows that the actual $\dot{V}$ decreased with a time constant of 8 s. Thus, for the MSFR model in Moltres, this work imposed a similar exponential decay term with a time constant of 8 s on the inflow Dirichlet boundary condition:

$$\dot{V} = \dot{V}_f + (\dot{V}_0 - \dot{V}_f)e^{-t/8}, \tag{6.5}$$

where

$$\dot{V}_f = \text{final volumetric flow rate} = 0.25862\ \text{m}^3{\cdot}\text{s}^{-1},$$

$$\dot{V}_0 = \text{initial volumetric flow rate} = 4.5\ \text{m}^3{\cdot}\text{s}^{-1}.$$

The reduced $\dot{V}$ also decreases the heat transfer rate between the primary and intermediate loop through the heat exchanger as the heat transfer coefficient h is dependent on the $\dot{V}$. For this loss of flow transient, Fiorina et al. [10] intended to focus on the primary loop and assumed that only the pumps in the primary loop failed.

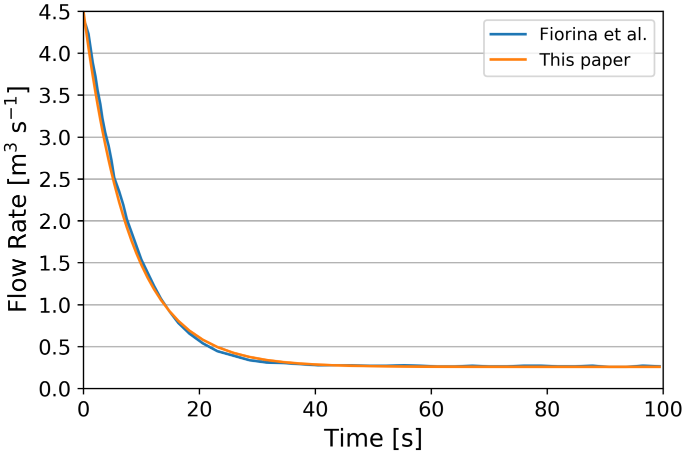

Figure 6.15: The change in flow rate in the Polimi and TUDelft models and the imposed flow rate in Moltres.

An issue arose pertaining to the turbulent viscosity μ_t as a function of v. This simple approximation, in which μ_t being directly proportional to v, causes the results from Moltres to differ significantly compared with the Polimi and TUDelft models. The difference is due to buoyancy-driven flow contributing to turbulence; the turbulent energy k equation in COMSOL's k-ϵ model has an explicit source term from buoyancy effects [65]. Another point to note is the Reynolds number remains constant if μ and v decrease in tandem. This preserves the existence of the recirculation zone in the core and it is at odds with the results from the Polimi and TUDelft models, which show that the recirculation zones disappear during the loss of flow transient. The current work circumvented this issue by retaining fixed fractions of the initial $\mu_{t,0}$ regardless of the final flow velocity, according to the following equation:

$$\mu_t = \mu_c + (\mu_{t,0} - \mu_c)e^{-t/8} \tag{6.6}$$

where

$$\mu_c = \text{ fixed fraction of } \mu_{t,0} \text{ independent with time [Pa·s].}$$

This measure allowed for laminar flow to develop in the core and yielded results showing better qualitative agreement with those from the Polimi and TUDelft models.

Figures 6.16 and 6.17 show the power output and average core temperature increase during the unprotected loss of flow transient in the Moltres, Polimi, and TUDelft models without decay heat modeling. The three sets of results from Moltres correspond to $\mu_c = \frac{1}{4}\mu_{t,0}, \frac{1}{2}\mu_{t,0},$ and $\frac{3}{4}\mu_{t,0}$. Although Moltres shows the same decreasing trend in power output, it failed to capture the exact individual features in the reactor response. In the Polimi and TUDelft models, Fiorina et al. [10] stated that after around $t = 15$ s, the “flow pattern changed in the core and the recirculation zones started to disappear”. The pocket of hot salt leaves the core and causes a sudden drop in the average core temperature. In Moltres, the wider peak in the average core temperature indicates a more gradual change in the flow pattern.

Figure 6.18 shows the flow patterns and temperature distribution in the core at $t = 300$ s in all three models. Figures 6.16, 6.17, and 6.18 combined highlight the difference between laminar flow in the Moltres model and buoyancy-driven flow in the other models, and its impact on the reactor response. They show that low-speed laminar flow is a poor substitute for buoyancy-driven flow in the context of the MSFR. It is particularly evident in the transition from high-speed turbulent flow to low-speed viscous flow as Moltres mispredicted the intermediate stages. As for μ_t, the need to fine-tune this parameter confirms that the uniform, function-based μ_t approach is inappropriate for safety analysis in a loss of flow accident.

The results from this transient inform our goals for Moltres: 1) implementing a proper turbulence model, and 2) developing a new heat exchanger feature that is compatible with the buoyancy-driven flow capabilities already present in Moltres.

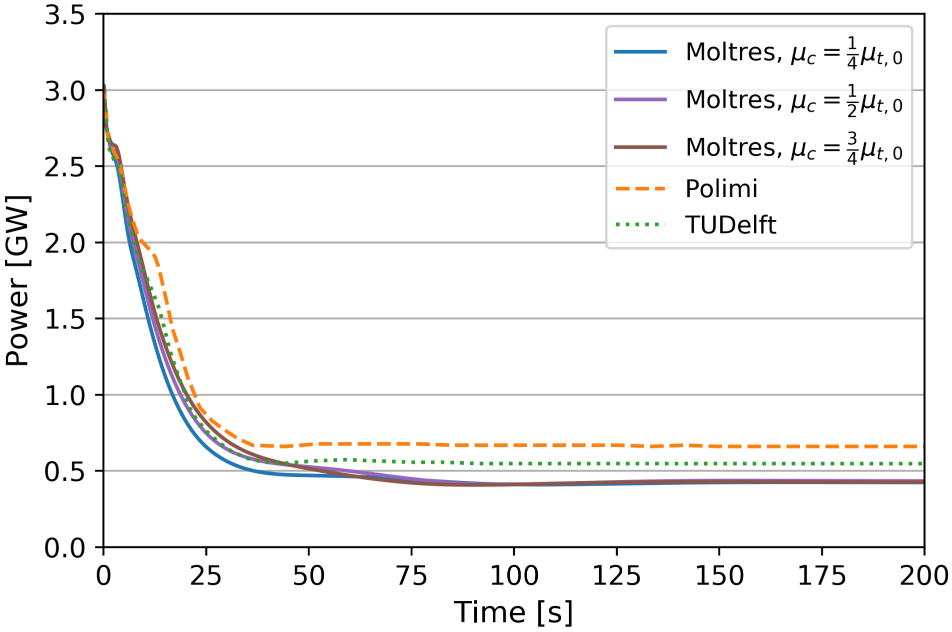

Figure 6.16: Power output during an unprotected loss of flow transient in the Moltres, Polimi, and TUDelft models [10].

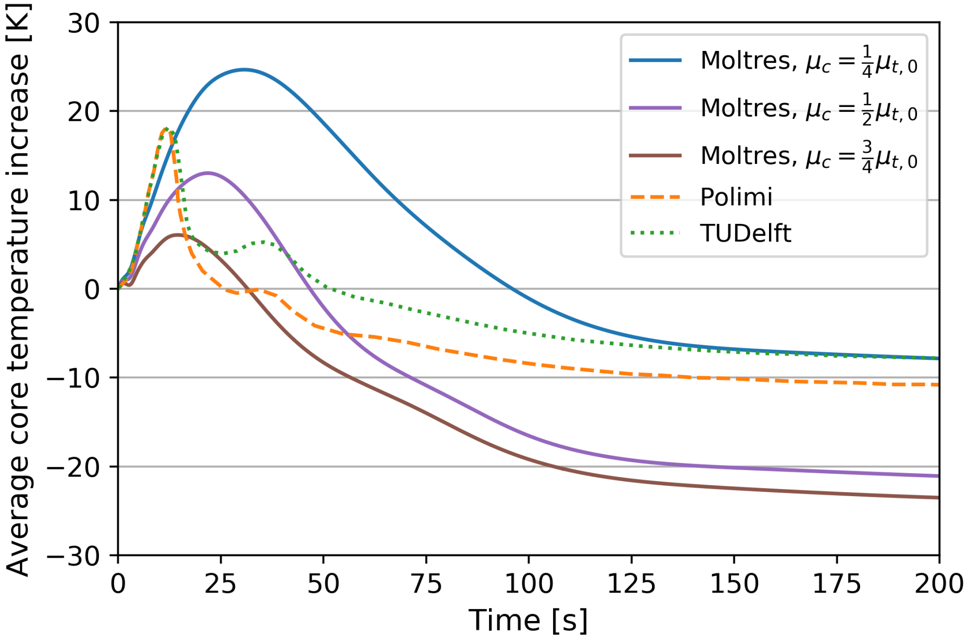

Figure 6.17: Average core temperature increase during an unprotected loss of flow transient in the Moltres, Polimi, and TUDelft models [10].

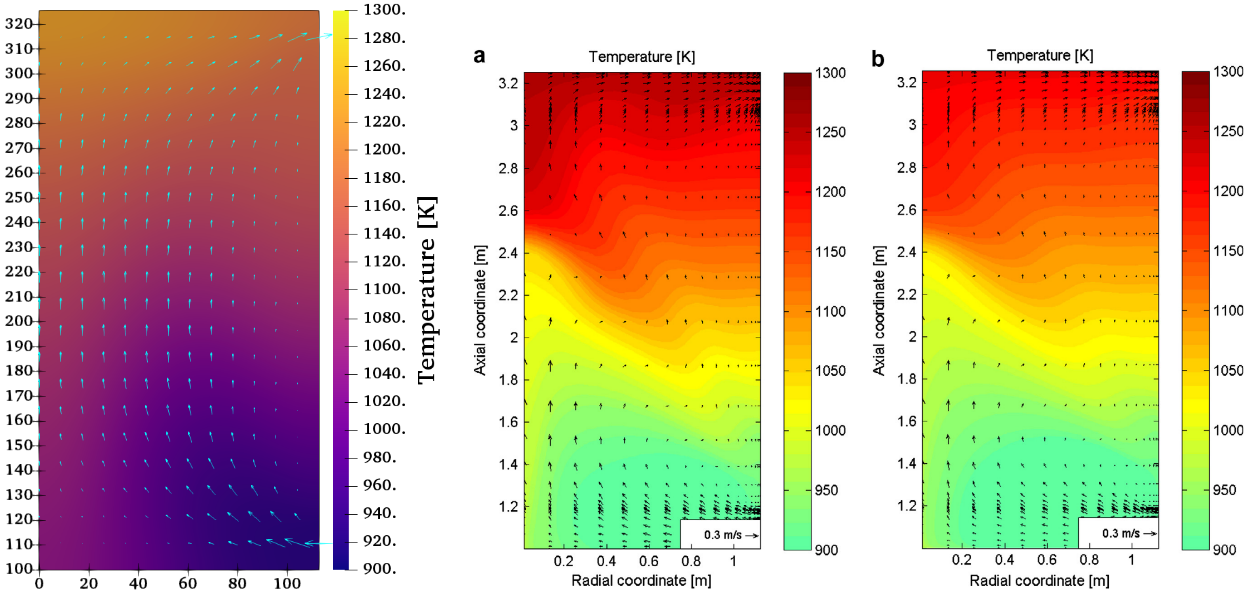

Figure 6.18: Temperature and velocity fields in the core at $t = 300$ s during a loss of flow transient in the Moltres ($\mu_c = \frac{1}{2}\mu_{t,0}$), Polimi, and TUDelft models.

Chapter 7

Conclusion

Unique phenomena in MSRs necessitate the development of new reactor safety analysis software. This thesis presents the latest developments in Moltres, namely coupling its existing neutron diffusion module to the incompressible Navier-Stokes module in MOOSE and developing a decay heat model for short-term transients. This work demonstrated and verified some of Moltres' current capabilities through a static-model neutronics study and a coupled neutronics/thermal-hydraulics safety analysis of the MSFR concept.

The neutronics study showed good agreement between Moltres and Serpent 2. With the relevant group constant data from Serpent 2, Moltres could accurately replicate the k_{eff}, β, α_T, and multi-group neutron flux results from Serpent 2. The k_{eff} estimates from Moltres were approximately 100 pcm higher for all measurements between 800 K and 1400 K. This discrepancy is notably smaller than the discrepancies observed in the neutron diffusion and SP3 models developed in OpenFOAM [60]. The β and α_T values from Moltres had 1.46% and 0.265% discrepancies, respectively, to Serpent 2's results. Lastly, the normalized six-group neutron fluxes from Moltres all had less than 1% discrepancy compared with Serpent 2. The results of this study extend the code-to-code verification of Moltres' neutron diffusion model with the six-group, fast-spectrum MSFR model.

Although Moltres currently lacks a proper turbulence model, the uniform turbulent viscosity μ_t approximation was accurate enough to reproduce most of the expected results for the MSFR steady-state and transient analyses. The steady-state temperature and velocity distributions showed many similarities in their shapes and magnitudes to the Polimi and TUDelft model results [10]. The uniform μ_t approximation was responsible for some differences in the flow in the recirculation zones. In turn, these differences in the recirculation zones resulted in differences in the loss of delayed neutrons to out-of-core emissions. The results with the decay heat model showed a slight flattening of the temperature distribution in the core that is in line with our expectations given the diffusion and advection of the decay heat precursors.

The unprotected reactivity insertion and loss of heat sink results showed the same trends Fiorina et al. [10] observed in their Polimi and TUDelft models. The small difference in the temperature reactivity coefficient accounted for the small difference in the magnitude of the peaks in power output and average core temperature increase. The differences between the pointwise heat exchanger in Moltres and the volumetric heat exchanger in the other two models required adjustments in the relationship between flow rate $\dot{V}$ and the heat transfer coefficient h from the original Dittus-Boelter correlation for the pump-initiated transients. Assuming a directly proportional relationship between μ_t and $\dot{V}$ yielded results in good agreement with the other two models for the pump overspeed transient. However, Moltres performed poorly in the loss of flow transient as this work could not incorporate buoyancy-driven flow and its associated effects on μ_t.

7.1 Future Work

Further research and development of Moltres should aim to rectify the issues mentioned in this thesis. This work has highlighted three main avenues for improvement. Firstly, a proper 2-D/3-D heat exchanger implementation would provide users with the option to simulate a fully closed 2-D/3-D coolant loop. If this were implemented, users would be able to use the Boussinesq approximation for buoyancy-driven flow capability in Moltres. Buoyancy-driven flow is a critical component in loss of forced flow scenarios which are important to reactor safety analyses.

Secondly, Moltres would benefit from a proper turbulence model such as k-ϵ [66] or k-ω [67]. Turbulence effects are significant in MSR designs and they inform optimization studies for improving flow patterns and eliminating local hotspots in eddies. The current work, particularly the loss of flow accident scenario, shows that simplifying assumptions for turbulence lead to erroneous results under flow conditions that deviate significantly from steady-state.

Lastly, a compressible Navier-Stokes model would be essential for modeling effects such as variable temperature-dependent density changes following a large reactivity insertion and finite wave propagation speeds in the salt. The presence of bubbles in the core from the gas sparging system increases fuel compressibility and enhances compressibility effects [62].

References

[1] A. J. McMichael, D. Campbell-Lendrum, S. Kovats, S. Edwards, P. Wilkinson, T. Wilson, R. Nicholls, S. Hales, F. Tanser, D. Le Sueur, M. Schlesinger, and N. Andronova, "Global Climate Change (Chapter 20)," in *Comparative Quantification of Health Risks*, pp. 1543–1649, World Health Organization, 2004. Library Catalog: www.unscn.org.

[2] IEA, "Global Energy and CO2 Status Report 2018," tech. rep., International Energy Agency, Paris, France, Mar. 2019.

[3] D. Petti, "The Future of Nuclear Energy in a Carbon-Constrained World," *Massachusetts Institute of Technology Energy Initiative (MITEI)*, p. 272, 2018.

[4] Massachusetts Institute of Technology, *The Future of nuclear power: an interdisciplinary MIT Study.* Boston MA: MIT, 2003. OCLC: 53208528.

[5] GIF, "A technology roadmap for generation IV nuclear energy systems," Tech. Rep. GIF-002-00, US DOE Nuclear Energy Research Advisory Committee and the Generation IV International Forum, 2002.

[6] NRC, "TRACE V5.0 User's Manual," tech. rep.

[7] T. H. Fanning, A. J. Brunett, and T. Sumner, "The SAS4A/SASSYS-1 Safety Analysis Code System, Version 5," Tech. Rep. ANL/NE-16/19, 1352187, Jan. 2017.

[8] E. E. Pettersen and K. Mikityuk, "Coupled multi-physics simulations of the Molten Salt Fast Reactor using coarse-mesh thermal-hydraulics and spatial neutronics," Master's thesis, MSc thesis, September 2016 (PDF), 2016.

[9] A. O. Graham, B. S. O. Collins, R. O. Salko Jr, R. Z. Taylor, and C. A. O. Gentry, "Development of Molten Salt Reactor Modeling and Simulation Capabilities in VERA," tech. rep., Oak Ridge National Lab. (ORNL), Oak Ridge, TN (United States), Sept. 2019.

[10] C. Fiorina, D. Lathouwers, M. Aufiero, A. Cammi, C. Guerrieri, J. L. Kloosterman, L. Luzzi, and M. E. Ricotti, "Modelling and analysis of the MSFR transient behaviour," *Annals of Nuclear Energy*, vol. 64, pp. 485–498, Feb. 2014.

[11] M. Aufiero, A. Cammi, O. Geoffroy, M. Losa, L. Luzzi, M. E. Ricotti, and H. Rouch, "Development of an OpenFOAM model for the Molten Salt Fast Reactor transient analysis," *Chemical Engineering Science*, vol. 111, pp. 390–401, May 2014.

[12] A. Lindsay, G. Ridley, A. Rykhlevskii, and K. Huff, "Introduction to Moltres: An application for simulation of Molten Salt Reactors," *Annals of Nuclear Energy*, vol. 114, pp. 530–540, Apr. 2018.

[13] D. R. Gaston, C. J. Permann, J. W. Peterson, A. E. Slaughter, D. Andr, Y. Wang, M. P. Short, D. M. Perez, M. R. Tonks, J. Ortensi, L. Zou, and R. C. Martineau, "Physics-based multiscale coupling for full core nuclear reactor simulation," *Annals of Nuclear Energy*, vol. 84, pp. 45–54, Oct. 2015.

[14] M. W. Rosenthal, P. R. Kasten, and R. B. Briggs, "Molten-Salt Reactors - History, Status, and Potential," *Nuclear Applications and Technology*, vol. 8, pp. 107–117, Feb. 1970.

[15] P. N. Haubenreich and J. R. Engel, "Experience with the Molten-Salt Reactor Experiment," *Nuclear Technology*, vol. 8, pp. 118–136, Feb. 1970.

[16] H. G. MacPherson, "The Molten Salt Reactor Adventure," *Nuclear Science and Engineering*, vol. 90, pp. 374–380, Aug. 1985.

[17] J. C. Gehin and J. J. Powers, "Liquid Fuel Molten Salt Reactors for Thorium Utilization," *Nuclear Technology*, vol. 194, pp. 152–161, May 2016.

[18] J. Smith and W. E. Simmons, "An assessment of a 2500 MWe molten chloride salt fast reactor," Tech. Rep. AEEW-R956, United Kindom Atomic Energy Authority, Aug. 1974.

[19] D. Heuer, E. Merle-Lucotte, M. Allibert, X. Doligez, and V. Ghetta, "Simulation Tools and New Developments of the Molten Salt Fast Reactor," *Revue Gnrale Nuclaire*, no. 6, pp. 95–100, 2010.

[20] L. Mathieu, D. Heuer, R. Brissot, C. Garzenne, C. Le Brun, D. Lecarpentier, E. Liatard, J.-M. Loiseaux, O. Mplan, E. Merle-Lucotte, A. Nuttin, E. Walle, and J. Wilson, "The thorium molten salt reactor: Moving on from the MSBR," *Progress in Nuclear Energy*, vol. 48, pp. 664–679, Sept. 2006.

[21] E. Merle, D. Heuer, M. Allibert, V. Ghetta, C. Brun, L. Mathieu, R. Brissot, and E. Liatard, "Optimized transition from the reactors of second and third generations to the Thorium Molten Salt Reactor," May 2007.

[22] GIF, "Generation IV International Forum 2008 Annual Report," tech. rep., Generation IV International Forum, 2008.

[23] EURATOM, "Final Report Summary - EVOL (Evaluation and Viability of Liquid Fuel Fast Reactor System) | Report Summary | EVOL | FP7| European Commission," Final report 249696, EURATOM, France, 2015.

[24] J. L. Kloosterman, "20 - Safety assessment of the molten salt fast reactor (SAMOFAR)," in *Molten Salt Reactors and Thorium Energy* (T. J. Dolan, ed.), pp. 565–570, Woodhead Publishing, 2017.

[25] D. LeBlanc, "Integral molten salt reactor," Feb. 2015.

[26] Transatomic Power Corporation, "Technical White Paper," White Paper 2.1, Transatomic Power Corporation, Cambridge, MA, United States, Nov. 2016.

[27] V. Ignatiev, O. Feynberg, I. Gnidoi, A. Merzlyakov, A. Surenkov, V. Uglov, A. Zagnitko, V. Subbotin, I. Sannikov, A. Toropov, V. Afonichkin, A. Bovet, V. Khokhlov, V. Shishkin, M. Kormilitsyn, A. Lizin, and A. Osipenko, "Molten salt actinide recycler and transforming

system without and with Th-U support: Fuel cycle flexibility and key material properties," *Annals of Nuclear Energy*, vol. 64, pp. 408–420, Feb. 2014.

[28] D. Zhang, L. Liu, M. Liu, R. Xu, C. Gong, J. Zhang, C. Wang, S. Qiu, and G. Su, "Review of conceptual design and fundamental research of molten salt reactors in China," *International Journal of Energy Research*, vol. 42, no. 5, pp. 1834–1848, 2018.

[29] A. Rykhlevskii, J. W. Bae, and K. D. Huff, "Modeling and simulation of online reprocessing in the thorium-fueled molten salt breeder reactor," *Annals of Nuclear Energy*, vol. 128, pp. 366–379, June 2019.

[30] B. M. Elsheikh, "Safety assessment of molten salt reactors in comparison with light water reactors," *Journal of Radiation Research and Applied Sciences*, vol. 6, pp. 63–70, Oct. 2013.

[31] I. K. Aji, T. Tatsuya, M. Kinoshita, and T. Okawa, "An Experimental and Numerical Study of Wall Effect on Freeze Valve Performance in a Molten Salt Reactor," *Journal of Nuclear Engineering and Radiation Science*, vol. 6, Apr. 2020.

[32] M. Brovchenko, D. Heuer, E. Merle, M. Allibert, V. Ghetta, A. Laureau, and P. Rubiolo, "Design-Related Studies for the Preliminary Safety Assessment of the Molten Salt Fast Reactor," *Nuclear Science and Engineering*, vol. 175, pp. 329–339, Nov. 2013.

[33] R. Yoshioka, M. Kinoshita, and I. Scott, "7 - Materials," in *Molten Salt Reactors and Thorium Energy* (T. J. Dolan, ed.), pp. 189–207, Woodhead Publishing, 2017.

[34] M. K. M. Ho, G. H. Yeoh, and G. Braoudakis, "Molten salt reactors," in *Materials and processes for energy: communicating current research and technological developments* (A. Mndez-Vilas, ed.), no. 1 in Energy Book Series, pp. 761–768, Badajoz, Spain: Formatex Research Center, 2013 ed., 2013. http://www.formatex.info/energymaterialsbook/ http://www.energymaterialsbook.org/chapters.html.

[35] T. Kamei, "Recent Research of Thorium Molten-Salt Reactor from a Sustainability Viewpoint," *Sustainability*, vol. 4, pp. 2399–2418, Sept. 2012.

[36] E. Merle-Lucotte, D. Heuer, M. Allibert, M. Brovchenko, N. Capellan, and V. Ghetta, "Launching the thorium fuel cycle with the Molten Salt Fast Reactor," in *Proceedings of ICAPP*, pp. 2–5, 2011.

[37] S. Grape and C. Hellesen, "10 - Nonproliferation and safeguards aspects of the MSR fuel cycle," in *Molten Salt Reactors and Thorium Energy* (T. J. Dolan, ed.), pp. 261–279, Woodhead Publishing, 2017.

[38] T. J. Dolan, "1 - Introduction," in *Molten Salt Reactors and Thorium Energy*, pp. 1–12, Woodhead Publishing, 2017.

[39] J. Krepel, U. Rohde, U. Grundmann, and F.-P. Weiss, "DYN3D-MSR spatial dynamics code for molten salt reactors," *Annals of Nuclear Energy*, vol. 34, pp. 449–462, June 2007.

[40] J. Kophazi, D. Lathouwers, and J. Kloosterman, "Development of a Three-Dimensional Time-Dependent Calculation Scheme for Molten Salt Reactors and Validation of the Measurement Data of the Molten Salt Reactor Experiment," *Nuclear Science and Engineering*, vol. 163, no. 2, pp. 118–131, 2009.

[41] A. Cammi, V. Di Marcello, L. Luzzi, V. Memoli, and M. E. Ricotti, “A multi-physics modelling approach to the dynamics of Molten Salt Reactors,” *Annals of Nuclear Energy*, vol. 38, pp. 1356–1372, June 2011.

[42] K. Nagy, D. Lathouwers, C. G. A. TJoen, J. L. Kloosterman, and T. H. J. J. van der Hagen, “Steady-state and dynamic behavior of a moderated molten salt reactor,” *Annals of Nuclear Energy*, vol. 64, pp. 365–379, Feb. 2014.

[43] D. Zhang, Z.-G. Zhai, A. Rineiski, Z. Guo, C. Wang, Y. Xiao, and S. Qiu, “COUPLE, A Time-Dependent Coupled Neutronics and Thermal-Hydraulics Code, and its Application to MSFR,” American Society of Mechanical Engineers Digital Collection, Nov. 2014.

[44] M. Zanetti, A. Cammi, C. Fiorina, and L. Luzzi, “A Geometric Multiscale modelling approach to the analysis of MSR plant dynamics,” *Progress in Nuclear Energy*, vol. 83, pp. 82–98, Aug. 2015.

[45] A. Laureau, D. Heuer, E. Merle-Lucotte, P. R. Rubiolo, M. Allibert, and M. Aufiero, “Transient coupled calculations of the Molten Salt Fast Reactor using the Transient Fission Matrix approach,” *Nuclear Engineering and Design*, vol. 316, pp. 112–124, May 2017.

[46] J. Leppanen, M. Pusa, T. Viitanen, V. Valtavirta, and T. Kaltiaisenaho, “The Serpent Monte Carlo code: Status, development and applications in 2013,” *Annals of Nuclear Energy*, vol. 82, pp. 142–150, Aug. 2014.

[47] E. Merle, “Concept of Molten Salt Fast Reactor,” 2017.

[48] M. Brovchenko, J.-L. Kloosterman, L. Luzzi, E. Merle, D. Heuer, A. Laureau, O. Feynberg, V. Ignatiev, M. Aufiero, A. Cammi, C. Fiorina, F. Alcaro, S. Dulla, P. Ravetto, L. Frima, D. Lathouwers, and B. Merk, “Neutronic benchmark of the molten salt fast reactor in the frame of the EVOL and MARS collaborative projects,” *EPJ Nuclear Sciences & Technologies*, vol. 5, p. 2, Jan. 2019.

[49] C. Fiorina, *The molten salt fast reactor as a fast spectrum candidate for thorium implementation*. PhD, Politecnico Di Milano, Mar. 2013.

[50] “Trelis (Version 16.5),” 2018.

[51] J. Leppnen, M. Aufiero, E. Fridman, R. Rachamin, and S. van der Marck, “Calculation of effective point kinetics parameters in the Serpent 2 Monte Carlo code,” *Annals of Nuclear Energy*, vol. 65, pp. 272–279, Mar. 2014.

[52] M. B. Chadwick, “ENDF/B-VII.1 Nuclear Data for Science and Technology: Cross Sections, Covariances, Fission Product Yields and Decay Data,” *Nuclear Data Sheets*, vol. 112, pp. 2887–2996, Dec. 2011.

[53] OECD/NEA, “The JEFF-3.1.2 Nuclear Data Library,” Tech. Rep. JEFF Report 24, OECD/NEA Data Bank, OECD/NEA, 2014.

[54] B. S. Kirk, J. W. Peterson, R. H. Stogner, and G. F. Carey, “libMesh: a C++ library for parallel adaptive mesh refinement/coarsening simulations,” *Engineering with Computers*, vol. 22, pp. 237–254, Dec. 2006.

[55] B. Satish, A. Shrirang, M. F. Adams, J. Brown, P. Brune, K. Buschelman, L. Dalcin, A. Dener, V. Eijkhout, W. D. Gropp, D. Karpeyev, D. Kaushik, M. G. Knepley, D. A. May, L. C. McInnes, R. T. Mills, T. Munson, K. Rupp, P. Sanan, B. F. Smith, S. Zampini, and H. Zhang, "PETSc Users Manual," Tech. Rep. ANL-95/11 - Revision 3.12, Argonne National Laboratory, 2019.

[56] J. W. Peterson, A. D. Lindsay, and F. Kong, "Overview of the Incompressible Navier-Stokes simulation capabilities in the MOOSE Framework," *arXiv:1710.08898 [math]*, Oct. 2017. arXiv: 1710.08898.

[57] S. M. Park, A. Rykhlevskii, and K. Huff, "Safety Analysis of Molten Salt Fast Reactor Fuel Composition using Moltres," in *Proceedings of GLOBAL International Fuel Cycle Conference*, (Seattle, WA, United States), American Nuclear Society, Sept. 2019.

[58] A. Lindsay, "Moltres, software for simulating Molten Salt Reactors," 2017. https://github.com/arfc/moltres.

[59] Y. Bartosiewicz and M. Duponcheel, "6.1.2 - Large-eddy simulation: Application to liquid metal fluid flow and heat transfer," in *Thermal Hydraulics Aspects of Liquid Metal Cooled Nuclear Reactors* (F. Roelofs, ed.), pp. 245–271, Woodhead Publishing, Jan. 2019.

[60] M. Aufiero, A. Cammi, C. Fiorina, J. Leppnen, L. Luzzi, and M. E. Ricotti, "An extended version of the SERPENT-2 code to investigate fuel burn-up and core material evolution of the Molten Salt Fast Reactor," *Journal of Nuclear Materials*, vol. 441, pp. 473–486, Oct. 2013.

[61] A. Moorthi, A. Kumar Sharma, and K. Velusamy, "A review of sub-channel thermal hydraulic codes for nuclear reactor core and future directions," *Nuclear Engineering and Design*, vol. 332, pp. 329–344, June 2018.

[62] E. Cervi, S. Lorenzi, A. Cammi, and L. Luzzi, "Development of a multiphysics model for the study of fuel compressibility effects in the Molten Salt Fast Reactor," *Chemical Engineering Science*, vol. 193, pp. 379–393, Jan. 2019.

[63] K. O. Ott and R. J. Neuhold, *Introductory nuclear reactor dynamics.* American Nuclear Society, Dec. 1985. Google-Books-ID: 3yVPAQAAIAAJ.

[64] F. W. Dittus and L. M. K. Boelter, "Heat transfer in automobile radiators of the tubular type," *University of California Publications in Engineering*, vol. 2, pp. 443–461, Oct. 1930.

[65] C. AB, "COMSOL Multiphysics," 2018.

[66] W. P. Jones and B. E. Launder, "The prediction of laminarization with a two-equation model of turbulence," *International Journal of Heat and Mass Transfer*, vol. 15, pp. 301–314, Feb. 1972.

[67] D. C. Wilcox, *Turbulence Modeling for CFD.* DCW Industries, 2006. Google-Books-ID: tFNNPgAACAAJ.